

# A coupled finite element-virtual element method for thermomechanical analysis of electronic packaging structures

Yanpeng Gong<sup>a,\*</sup>, Sishuai Li<sup>a</sup>, Fei Qin<sup>a</sup>, Yue Mei<sup>b,\*</sup>, Xiaoying Zhuang<sup>c,d</sup>,  
Timon Rabczuk<sup>e</sup>

<sup>a</sup>*Department of Mechanics, Beijing University of Technology, Beijing, 100124, China*

<sup>b</sup>*State Key Laboratory of Structural Analysis for Industrial Equipment, Department of Engineering Mechanics, International Research Center for Computational Mechanics, Dalian University of Technology, Dalian 116023, China*

<sup>c</sup>*Chair of Computational Science and Simulation Technology, Institute of Photonics, Department of Mathematics and Physics, Leibniz University Hannover, 30167 Hannover, Germany*

<sup>d</sup>*Department of Geotechnical Engineering, College of Civil Engineering, Tongji University, Shanghai, 200092, China*

<sup>e</sup>*Institute of Structural Mechanics, Bauhaus University Weimar, 99423 Weimar, Germany*

---

## Abstract

This study presents a finite element and virtual element (FE-VE) coupled method for thermomechanical analysis in electronic packaging structures. The approach partitions computational domains strategically, employing FEM for regular geometries to maximize computational efficiency and VEM for complex shapes to enhance geometric flexibility. Interface compatibility is maintained through coincident nodal correspondence, ensuring solution continuity across domain boundaries while reducing meshing complexity and computational overhead. Validation through electronic packaging applications demonstrates reasonable agreement with reference solutions and acceptable convergence characteristics across varying mesh densities. The method effectively captures thermal distributions and stress concentrations in multi-material systems, establishing a practical computational framework for elec-

---

\*Corresponding author

*Email addresses:* `yanpeng.gong@bjut.edu.cn` (Yanpeng Gong),  
`meiyue@dlut.edu.cn` (Yue Mei)

tronic packaging analysis involving complex geometries. Source codes are available at <https://github.com/yanpeng-gong/FeVeCoupled-ElectronicPackaging>.

*Keywords:* Virtual element method, FE-VE coupling, Thermomechanical analysis, Electronic packaging, Geometric multi-scale structures

---

## 1. Introduction

Modern electronic devices face increasing thermal management challenges due to rising chip integration density and power density, which generate elevated operating temperatures that degrade performance and reduce service life [1]. The multi-material nature of electronic packaging exacerbates these challenges, as thermal expansion coefficient mismatches between heterogeneous materials create substantial thermal stresses during temperature cycling [2]. These thermomechanical stresses contribute to critical reliability failures, including solder joint cracking [3], wire bond fatigue, and substrate delamination [4]. Recent studies indicate that thermomechanical effects account for over 55% of electronic device failures in advanced 3D integrated circuits [5], underscoring the critical importance of accurate thermal and thermomechanical analysis for electronic packaging reliability assessment.

Numerical simulation methods have become essential for electronic packaging reliability analysis, offering cost-effective and reliable assessment capabilities. However, thermomechanical coupling analysis in electronic packaging faces significant computational challenges due to multi-scale geometric features and complex material interfaces in modern designs. Researchers have developed various numerical approaches to address these challenges, including the Finite Element Method (FEM) [6], Boundary Element Method (BEM) [7], Isogeometric BEM [3, 8, 9], FEM-BEM coupling [10, 11], Phase Field scheme [12, 13], Scientific Machine Learning [14], Finite Difference Method [15] and Finite Volume Method [16]. Recent advances have also introduced specialized approaches: Inamdar et al. [17] developed physics-based Digital Twin modeling for thermomechanical degradation prediction; Feng et al. [18] proposed smoothed finite element algorithms for electro-thermal-mechanical coupling; and Wang et al. [19] integrated machine learning approaches for thermal stress reduction strategies.

With the advancement of commercial finite element software packages (ANSYS, Abaqus, COMSOL), FEM has become the predominant numerical method for thermal and thermomechanical analysis in electronic devices.

Recent applications demonstrate its effectiveness across diverse packaging technologies: Wang et al. [20] integrated finite element analysis with Taguchi optimization to investigate thermal stress in chip-scale package LEDs; Liu et al. [21] developed coupled thermomechanical simulation techniques using Spectral Element Time Domain methods; Gong et al. [22] employed COM-SOL Multiphysics for three-dimensional multi-chip module BGA modeling to address thermal hotspot issues; and advanced constitutive models such as the Anand model have been applied [23] to characterize SAC305 solder behavior in 3D packaging under thermal cycling from -100 °C to 120 °C.

Despite FEM’s mature theoretical framework and high computational accuracy for regular structures with quality meshes, it faces significant challenges when analyzing multi-scale geometric configurations. Complex geometries require extensive mesh refinement and careful element partitioning to prevent distortion, while geometric scale variations necessitate transitional meshes that can generate millions of elements. This dramatically increases computational cost and may cause convergence issues. The Virtual Element Method (VEM) addresses these limitations through enhanced geometric flexibility [24]. VEM accommodates arbitrary polygonal elements that simplify complex geometry discretization and enables local refinement through non-conforming meshes without compromising overall mesh quality. This capability reduces element count and computational cost while preserving solution accuracy, making VEM particularly suitable for multi-scale problems where traditional meshing approaches become prohibitively expensive.

The VEM was first introduced by Beirão da Veiga et al. [25] for Poisson’s equation and has since expanded across multiple engineering applications. Early validation studies by Artioli et al. [26] demonstrated VEM’s accuracy through computational benchmarks including Cook’s membrane tests. Subsequent research [27, 28, 29, 30] has confirmed VEM’s geometric robustness and convergence properties for arbitrary element shapes, including non-convex configurations. VEM applications have extended beyond linear elasticity to encompass hyperelastic materials [31, 32], contact mechanics [33, 34], elastoplasticity [35, 36], and phase field fracture modeling [37]. Dhanush et al. [38] pioneered VEM implementation for thermomechanical coupling using Abaqus UEL framework. Recently, Gong et al. [24] analyzed thermoelastic problems using VEM, presenting both the standard virtual element method and a stabilization-free virtual element method [39] for thermomechanical behavior analysis in electronic packaging structures with geometric multi-scale features. Their work demonstrated that VEM’s polygonal mesh flexibility en-

ables localized mesh modifications without affecting global mesh structure, making it particularly effective for electronic packaging reliability analysis involving complex geometries. However, VEM requires projection operators and stabilization terms that increase algorithmic complexity and may result in higher local computational costs compared to conventional FEM.

This work proposes an FE-VE coupled methodology that strategically combines the computational advantages of both methods for problems involving multi-scale geometric features. The approach employs VEM with polygonal discretization in geometrically complex regions, leveraging its tolerance for arbitrary element shapes, while utilizing standard quadrilateral finite elements in regular domains to exploit FEM's computational efficiency. This hybrid strategy balances accuracy and computational cost by applying each method where it performs optimally. The coupled approach is applied to thermomechanical analysis of electronic packaging structures and validated through analytical benchmarks and practical case studies, demonstrating its effectiveness for capturing thermal distributions and stress concentrations in multi-material systems. The framework addresses computational challenges in multi-scale thermomechanical problems by strategically combining FEM's efficiency in structured regions with VEM's geometric flexibility in irregular domains.

The remainder of this paper is organized as follows: Sec. 2 presents the mathematical formulation for thermomechanical coupling, including governing equations and weak forms. Sec. 3 establishes the discrete framework for both FEM and VEM approaches, followed by a comparative analysis. Sec. 4 describes the FE-VE coupling methodology, including domain decomposition and interface treatment. Sec. 5 validates the proposed approach through numerical examples, and Sec. 6 provides concluding remarks.

## 2. Mathematical formulation of thermomechanical coupling

We consider a continuous domain  $\Omega$  subjected to body force  $\mathbf{f}$ , as illustrated in Fig. 1. The domain boundary  $\partial\Omega$  is partitioned into two pairs of disjoint regions for the thermomechanical problem

$$\partial\Omega = \partial\Omega_D \cup \partial\Omega_N, \quad \partial\Omega_D \cap \partial\Omega_N = \emptyset, \quad (1)$$

$$\partial\Omega = \partial\Omega_T \cup \partial\Omega_q, \quad \partial\Omega_T \cap \partial\Omega_q = \emptyset, \quad (2)$$

where  $\partial\Omega_D$  and  $\partial\Omega_N$  represent the displacement and traction boundaries for the mechanical field, while  $\partial\Omega_T$  and  $\partial\Omega_q$  denote the temperature and heat



flux boundaries for the thermal field, respectively. The governing equations for both physical fields are established below.

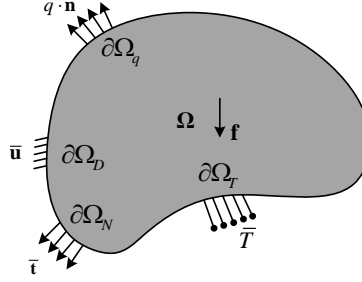


Figure 1: Schematic of the thermoelastic coupling problem domain.

### 2.1. Governing equations

For the steady-state heat conduction problem without heat sources, the governing equation takes the form

$$\nabla \cdot (\lambda \nabla T) = 0, \quad (3)$$

where  $\lambda$  is the thermal conductivity and  $T$  is the temperature field. The boundary conditions on  $\partial\Omega = \partial\Omega_T \cup \partial\Omega_q$  are expressed as

$$T(\mathbf{x}) = \bar{T}, \quad \forall \mathbf{x} \in \partial\Omega_T, \quad (4)$$

$$-\lambda \nabla T(\mathbf{x}) \cdot \mathbf{n} = \bar{q}, \quad \forall \mathbf{x} \in \partial\Omega_q, \quad (5)$$

where  $\bar{q}$  represents the prescribed heat flux (positive for outward flux) and  $\mathbf{n}$  is the outward unit normal vector.

For the thermoelastic problem, the governing equation is

$$\nabla \cdot \boldsymbol{\sigma} + \mathbf{f} = 0, \quad (6)$$

where  $\boldsymbol{\sigma}$  is the Cauchy stress tensor. The constitutive relation considering thermal strain is

$$\boldsymbol{\sigma} = \mathbb{D} : (\boldsymbol{\varepsilon} - \boldsymbol{\varepsilon}_{\text{th}}), \quad (7)$$

where  $\mathbb{D}$  is the fourth-order elasticity tensor,  $\boldsymbol{\varepsilon}$  is the strain tensor, and  $\boldsymbol{\varepsilon}_{\text{th}}$  is the thermal strain. The strain tensor is defined as

$$\boldsymbol{\varepsilon}(\mathbf{u}) = \frac{1}{2} (\nabla \mathbf{u} + (\nabla \mathbf{u})^T). \quad (8)$$

The thermal strain is expressed as

$$\boldsymbol{\varepsilon}_{\text{th}} = \alpha(T - T_0)\mathbf{I}, \quad (9)$$

where  $\mathbf{I}$  is the identity tensor,  $\alpha$  is the coefficient of thermal expansion, and  $T_0$  is the reference temperature.

The boundary conditions on  $\partial\Omega = \partial\Omega_D \cup \partial\Omega_N$  are expressed as

$$\mathbf{u}(\mathbf{x}) = \bar{\mathbf{u}}, \quad \forall \mathbf{x} \in \partial\Omega_D, \quad (10)$$

$$\boldsymbol{\sigma}(\mathbf{x})\mathbf{n} = \bar{\mathbf{t}}, \quad \forall \mathbf{x} \in \partial\Omega_N, \quad (11)$$

where  $\bar{\mathbf{u}}$  and  $\bar{\mathbf{t}}$  represent the prescribed displacement and traction vectors, respectively.

## 2.2. Weak formulation

The weak form of the thermal equilibrium equation is

$$a_T(T, \varphi) = \ell_T(\varphi), \quad (12)$$

where  $\varphi$  is the test function (virtual temperature variation). The corresponding bilinear and linear forms are defined as

$$a_T(T, \varphi) = \lambda \int_{\Omega} \nabla T \cdot \nabla \varphi \, d\Omega, \quad (13)$$

$$\ell_T(\varphi) = \int_{\partial\Omega_q} \varphi \bar{q} \, d\Gamma. \quad (14)$$

The thermoelastic equilibrium equation becomes: find  $\mathbf{u} \in V_u$  such that

$$a_u(\mathbf{u}, \mathbf{v}) = \ell(\mathbf{v}), \quad \forall \mathbf{v} \in V_u^0, \quad (15)$$

where  $\mathbf{u}$  is the displacement field,  $\mathbf{v}$  is the test function,  $V_u$  is the space of admissible displacement functions satisfying essential boundary conditions, and  $V_u^0$  is the space of test functions satisfying homogeneous displacement boundary conditions. The corresponding bilinear and linear forms are defined as [40]

$$a_u(\mathbf{u}, \mathbf{v}) = \int_{\Omega} \boldsymbol{\varepsilon}(\mathbf{u}) : \mathbb{D} : \boldsymbol{\varepsilon}(\mathbf{v}) \, d\Omega, \quad (16)$$

$$\ell(\mathbf{v}) = \int_{\Omega} \mathbf{v} \cdot \mathbf{f} \, d\Omega + \int_{\partial\Omega_N} \mathbf{v} \cdot \bar{\mathbf{t}} \, d\Gamma + \int_{\Omega} \boldsymbol{\varepsilon}(\mathbf{v}) : \mathbb{D} : \boldsymbol{\varepsilon}_{\text{th}} \, d\Omega. \quad (17)$$

The linear form includes contributions from body forces, surface tractions, and thermal loads, with the last term in Eq. (17) representing the thermo-mechanical coupling through thermal expansion effects.

### 3. Numerical discretization methods

#### 3.1. Finite element formulation

##### 3.1.1. Thermal analysis

For the finite element discretization of the thermal problem, we employ the weak formulation established in Sec. 2.2. The domain is discretized into finite elements such that  $\Omega \equiv \text{int}(\bigcup_i E_i)$ , where element  $E_i$  is chosen as a four-node quadrilateral isoparametric element.

According to the Galerkin method, the test functions are chosen as the shape functions, i.e.,  $\varphi_j = N_j$  for  $j = 1, 2, 3, 4$ . The temperature field within each element is approximated as

$$T(\mathbf{x}) = \sum_{i=1}^4 N_i(\xi, \eta) T_i, \quad (18)$$

where  $N_i(\xi, \eta)$  are the bilinear shape functions and  $(\xi, \eta) \in [-1, 1]$  index local coordinates,  $T_i$  are the nodal temperatures at the element nodes.

The element-wise weak form can be written as

$$\sum_{i=1}^4 \int_E \lambda (\nabla N_j)^T \cdot \nabla N_i \, dE T_i = - \int_{\partial E} N_j \bar{q} \, d\Gamma. \quad (19)$$

This leads to the standard finite element matrix equation for each element

$$\mathbf{K}_{\text{FE}}^{th,E} \mathbf{T}^E = \mathbf{f}_{\text{FE}}^{th,E}, \quad (20)$$

where the element thermal stiffness matrix is defined as

$$\mathbf{K}_{\text{FE}}^{th,E} = \int_E \lambda \mathbf{B}_T^T \mathbf{B}_T \, dE \quad (21)$$

and the element thermal load vector is

$$\mathbf{f}_{\text{FE}}^{th,E} = - \int_{\partial E \cap \partial \Omega_q} \mathbf{N}^T \bar{q} \, d\Gamma, \quad (22)$$

where  $\mathbf{B}_T$  is the thermal gradient matrix and  $\mathbf{N} = [N_1, N_2, N_3, N_4]^T$  is the shape function vector. The vector  $\mathbf{f}_{\text{FE}}^{th,E}$  represents the equivalent nodal loads due to prescribed heat flux boundary conditions.

The integrals are evaluated using  $2 \times 2$  Gaussian quadrature in the local coordinate system

$$\mathbf{K}_{\text{FE}}^{th,E} = \sum_{p=1}^2 \sum_{q=1}^2 w_p w_q \lambda(\xi_p, \eta_q) \mathbf{B}_T^T(\xi_p, \eta_q) \mathbf{B}_T(\xi_p, \eta_q) \det(\mathbf{J}(\xi_p, \eta_q)), \quad (23)$$

where  $w_p$  and  $w_q$  are the Gaussian weights ( $w_1 = w_2 = 1.0$ ),  $(\xi_p, \eta_q)$  are the integration points ( $\xi_1 = \eta_1 = -1/\sqrt{3}$ ,  $\xi_2 = \eta_2 = 1/\sqrt{3}$ ), and  $\det(\mathbf{J})$  is the determinant of the Jacobian matrix.

The global system of equations is assembled from the element contributions using standard finite element assembly

$$\mathbf{K}_{\text{FE}}^{th} \mathbf{T} = \mathbf{f}_{\text{FE}}^{th}, \quad (24)$$

where the global thermal stiffness matrix and load vector are assembled as

$$\mathbf{K}_{\text{FE}}^{th} = \mathcal{A}_E \mathbf{K}_{\text{FE}}^{th,E}, \quad (25)$$

$$\mathbf{f}_{\text{FE}}^{th} = \mathcal{A}_E \mathbf{f}_{\text{FE}}^{th,E}, \quad (26)$$

where  $\mathcal{A}$  denotes the standard assembly operator that maps element degrees of freedom (Dofs) to global Dofs according to element connectivity.

### 3.1.2. Thermoelastic analysis

For the finite element discretization of the mechanical problem, we employ the weak formulation established in Sec. 2.2. Within each element, the displacement field is interpolated using the same shape functions as the thermal analysis

$$\mathbf{u}(\mathbf{x}) = \sum_{i=1}^4 N_i(\xi, \eta) \mathbf{u}_i = \mathbf{N} \mathbf{u}^E, \quad (27)$$

where  $\mathbf{u}_i$  is the  $i$ th nodal displacement vector,  $\mathbf{u}^E = [\mathbf{u}_1^T, \mathbf{u}_2^T, \mathbf{u}_3^T, \mathbf{u}_4^T]^T$  is the element displacement vector, and  $\mathbf{N}$  is the shape function matrix

The strain-displacement relationship is given by

$$\boldsymbol{\varepsilon} = \mathbf{B}_u \mathbf{u}^E, \quad (28)$$

where  $\mathbf{B}_u$  is the strain-displacement matrix that relates the element nodal displacements to the strain components. The matrix  $\mathbf{B}_u$  contains the derivatives of the shape functions with respect to the global coordinates, obtained through the coordinate transformation using the Jacobian matrix.

The element mechanical stiffness matrix is computed using Gaussian quadrature

$$\mathbf{K}_{\text{FE}}^{u,E} = \int_E \mathbf{B}_u^T \mathbb{D} \mathbf{B}_u \, dE = \sum_{p=1}^2 \sum_{q=1}^2 w_p w_q \mathbf{B}_u^T(\xi_p, \eta_q) \mathbb{D} \mathbf{B}_u(\xi_p, \eta_q) \det(\mathbf{J}(\xi_p, \eta_q)). \quad (29)$$

The element load vector includes contributions from external loads and thermal effects

$$\mathbf{F}_{\text{FE}}^{u,E} = \mathbf{F}_{\text{ext}}^E + \mathbf{F}_{\text{FE}}^{th,E}, \quad (30)$$

where  $\mathbf{F}_{\text{ext}}^E$  represents the external load vector from body forces and surface tractions.

After assembly, the global system of equations becomes

$$\mathbf{K}_{\text{FE}}^u \mathbf{u} = \mathbf{F}_{\text{FE}}^u, \quad (31)$$

where  $\mathbf{K}_{\text{FE}}^u$  and  $\mathbf{F}_{\text{FE}}^u$  are assembled from the element contributions.

The thermal load vector, arising from the thermomechanical coupling, is computed as

$$\mathbf{F}_{\text{FE}}^{th} = \sum_E \int_E \mathbf{B}_u^T \mathbb{D} \boldsymbol{\varepsilon}_{\text{th}} \, dE = \sum_E \int_E \mathbf{B}_u^T \mathbb{D} \alpha (T - T_0) \mathbf{I} \, dE, \quad (32)$$

where  $\mathbf{I} = [1, 1, 0]^T$  is the thermal expansion vector for plane stress/strain conditions,  $T(\xi, \eta) = \sum_{i=1}^4 N_i(\xi, \eta) T_i$  is the temperature field obtained from the thermal analysis.

### 3.2. Virtual element formulation

#### 3.2.1. Thermal analysis

For the heat conduction problem, the scalar virtual element function space is defined as

$$\mathcal{V}_T = \{T \in \mathcal{H}^1(\Omega) : T|_E \in \mathcal{V}_T^h(E) \text{ for all } E, T = \bar{T} \text{ on } \partial\Omega_T\}, \quad (33)$$

where the local virtual element space on element  $E$  is defined as

$$\mathcal{V}_T^h(E) = \{T \in \mathcal{H}^1(E) : \Delta T = 0 \text{ in } E, T|_{\partial E} \in \mathcal{P}_k(\partial E)\}. \quad (34)$$

Here,  $\mathcal{P}_k(\partial E)$  denotes the space of polynomial functions of degree not exceeding  $k$  on the boundary of element  $E$ . In this work,  $k = 1$  is chosen,

leading to linear virtual elements. The scaled polynomial space  $\mathcal{P}_k(E)$  on element  $E$  is spanned by the monomial basis. For  $k = 1$ , the polynomial space is [38]

$$\mathcal{P}_1(E) = \{p_1, p_2, p_3\} = \text{span}\{1, \zeta, \wp\}, \quad (35)$$

where the scaled coordinates  $\zeta$  and  $\wp$  are defined as [39]

$$\zeta = \frac{x - \bar{x}}{h_E}, \quad \wp = \frac{y - \bar{y}}{h_E}, \quad (36)$$

in which  $\bar{\mathbf{x}} = (\bar{x}, \bar{y})$  represents the centroid of element  $E$ , and  $h_E$  denotes the characteristic element size defined as the maximum distance between any two nodes in element  $E$ .

Since the element shape functions do not have explicit expressions, a projection operator is defined to compute the bilinear forms. The approximate function space  $\mathcal{V}_T^h(E)$  on element  $E$  is mapped to the polynomial space  $\mathcal{P}_k(E)$  through the projection operator

$$\Pi : \mathcal{V}_T^h(E) \rightarrow \mathcal{P}_k(E), \quad (37)$$

which satisfies the orthogonality condition

$$a_T^E(\psi - \Pi\psi, p) = 0, \quad \forall p \in \mathcal{P}_k(E) \quad (38)$$

where  $\psi$  is the basis function of  $\mathcal{V}_T^h(E)$ .

Expanding Eq. (38) yields

$$\int_E \nabla(\Pi\psi) \cdot \nabla p \, dE = \int_E \nabla\psi \cdot \nabla p \, dE. \quad (39)$$

The matrix representation  $\tilde{\Pi}$  of the projection operator  $\Pi$  can be obtained by [41, 38]

$$\tilde{\Pi} = \mathbf{G}^{-1} \mathbf{B}, \quad (40)$$

where

$$\mathbf{G}_{\alpha\beta} = \lambda \int_E \nabla p_\alpha \cdot \nabla p_\beta \, dE \quad (41)$$

$$\mathbf{B}_{i\alpha} = \lambda \int_{\partial E} \psi_i \cdot (\nabla p_\alpha) \mathbf{n} \, d\Gamma \quad (42)$$

where  $\alpha, \beta = 1, 2, 3$  index the polynomial basis functions  $p_\alpha \in \mathcal{P}_1(E)$ , and  $i = 1, 2, \dots, n_v$  indexes the basis function  $\psi_i$  of  $\mathcal{V}_T^h(E)$  corresponding to the  $i$ -th vertex of the polygonal element.

For the temperature field  $T^h$ , the bilinear form on each element can be decomposed as

$$\begin{aligned} a_T^E(T^h, \varphi^h) &= a_T^E(T^h - \Pi T^h + \Pi T^h, \varphi^h - \Pi \varphi^h + \Pi \varphi^h) \\ &= a_T^E(\Pi T^h, \Pi \varphi^h) + a_T^E(T^h - \Pi T^h, \varphi^h - \Pi \varphi^h). \end{aligned} \quad (43)$$

In Eq. (43), the first term on the right-hand side represents the consistency term computed from the integral of projected functions in element  $E$ . The second term represents the stabilization term that accounts for the energy associated with the non-polynomial component of the solution.

The element thermal stiffness matrix consists of two parts

$$\mathbf{K}_{\text{VE}}^{th,E} = \mathbf{K}_E^{th,c} + \mathbf{K}_E^{th,s}, \quad (44)$$

where  $\mathbf{K}_E^{th,c}$  is the consistency stiffness matrix and  $\mathbf{K}_E^{th,s}$  is the stabilization stiffness matrix.

For the heat conduction problem, the matrix  $\mathbf{D}_{n_v \times n_k}$  represents the evaluation of polynomial basis functions  $p_\alpha$  at the degrees of freedom locations

$$\mathbf{D}_{j\beta} = \text{dof}_j(p_\beta), \quad j = 1, 2, \dots, n_v, \quad \beta = 1, 2, 3 \quad (45)$$

where  $\text{dof}_j(\cdot)$  denotes the  $j$ -th degree of freedom value (nodal evaluation for the temperature field),  $n_v$  is the number of vertices for the polygonal element, and  $n_k = 3$  is the dimension of the polynomial space  $\mathcal{P}_1(E)$ .

The stabilization stiffness matrix is expressed as [41]

$$\mathbf{K}_E^{th,s} = \tau^h \text{tr} \left( \mathbf{K}_E^{th,c} \right) (\mathbf{I} - \mathbf{\Pi})^T (\mathbf{I} - \mathbf{\Pi}), \quad (46)$$

where the projection operator is given by

$$\mathbf{\Pi} = \mathbf{D} \tilde{\mathbf{\Pi}}, \quad (47)$$

representing the mapping from the VEM space to the degrees of freedom space through the polynomial space. Here  $\text{tr}(\cdot)$  denotes the trace operator, and  $\mathbf{I}$  is the  $n_v \times n_v$  identity matrix,  $\tau^h = 1/2$  is the stabilization parameter [41]. According to Reference [26], VEM results show limited sensitivity to the stabilization parameter  $\tau^h$ . The numerical solution maintains stable accuracy and convergence across a wide range of  $\tau^h$  values, with optimal performance achieved at  $\tau^h = 1/2$ .

### 3.2.2. Thermoelastic analysis

For elasticity problems, the global virtual element space is defined as

$$\mathcal{V}_{\mathbf{u}} = \{ \mathbf{v} \in [\mathcal{H}^1(\Omega)]^2 : \mathbf{v}|_E \in \mathcal{V}_{\mathbf{u}}^h(E) \text{ for all } E, \mathbf{v} = \bar{\mathbf{u}} \text{ on } \partial\Omega_D \}, \quad (48)$$

where  $\mathbf{v}$  represents any vector function in the space, and the local virtual element space on element  $E$  is defined as [42]

$$\begin{aligned} \mathcal{V}_{\mathbf{u}}^h(E) := \Big\{ & \mathbf{v}^h \in [\mathcal{H}^1(E)]^2 : \mathbf{v}^h|_{\partial E} \in [\mathcal{C}^0(\partial E)]^2, \\ & \mathbf{v}^h|_E \in [\mathbf{M}_k(E)]^2, \\ & \Delta \mathbf{v}^h|_E \in [\mathbf{M}_{k-2}(E)]^2 \Big\}, \end{aligned} \quad (49)$$

where  $\mathbf{v}^h$  represents the discrete vector function within the element.

For interpolation order  $k = 1$ , the constraint effectively requires  $\Delta \mathbf{v}^h = 0$  within each element, since  $\mathbf{M}_{-1}(E)$  contains only the zero polynomial. The local polynomial space  $\mathbf{M}_1(E)$  consists of the following basis functions [43]

$$\mathbf{M}_1(E) = \{ \mathbf{m}_1, \mathbf{m}_2, \mathbf{m}_3, \mathbf{m}_4, \mathbf{m}_5, \mathbf{m}_6 \}, \quad (50)$$

where

$$\mathbf{m}_1 = \begin{pmatrix} 1 \\ 0 \end{pmatrix}, \mathbf{m}_2 = \begin{pmatrix} 0 \\ 1 \end{pmatrix}, \mathbf{m}_3 = \begin{pmatrix} -\wp \\ \zeta \end{pmatrix}, \mathbf{m}_4 = \begin{pmatrix} \wp \\ \zeta \end{pmatrix}, \mathbf{m}_5 = \begin{pmatrix} \zeta \\ 0 \end{pmatrix}, \mathbf{m}_6 = \begin{pmatrix} 0 \\ \wp \end{pmatrix}.$$

For a polygon with  $n_v$  vertices, the Dof for the two-dimensional vector problem are  $2n_v$ . The local virtual element space  $\mathcal{V}_{\mathbf{u}}^h(E)$  is mapped to the polynomial space  $\mathbf{M}_k(E)$  through the projection operator

$$\Pi^\nabla : \mathcal{V}_{\mathbf{u}}^h(E) \rightarrow \mathbf{M}_k(E). \quad (51)$$

Assuming  $\phi$  is the basis function of  $\mathcal{V}_{\mathbf{u}}^h(E)$ , the projection operator satisfies the orthogonality condition,

$$a_u^E(\phi - \Pi^\nabla \phi, \mathbf{m}) = 0, \quad \forall \mathbf{m} \in \mathbf{M}_k(E) \quad (52)$$

where the local bilinear form is defined as

$$a_u^E(\phi, \mathbf{m}) = \int_E \boldsymbol{\varepsilon}(\phi) : \mathbb{D} : \boldsymbol{\varepsilon}(\mathbf{m}) \, dE. \quad (53)$$



According to Eq. (52), we can obtain

$$a_u^E(\boldsymbol{\phi}, \mathbf{m}) = a_u^E(\Pi^\nabla \boldsymbol{\phi}, \mathbf{m}), \quad \forall \mathbf{m} \in \mathbf{M}_k(E) \quad (54)$$

Based on the references [31, 44],  $\Pi^\nabla \boldsymbol{\phi}$  can be expressed as a linear combination of the polynomial basis functions  $\mathbf{m}$  in  $\mathbf{M}_k(E)$ . Thus,

$$\Pi^\nabla \boldsymbol{\phi} = \mathbf{m} \tilde{\Pi}^{*\nabla}, \quad (55)$$

By using Eq. (54), we can derive the following matrix equation to solve for  $\tilde{\Pi}^{*\nabla}$ ,

$$\mathbf{M} \tilde{\Pi}^{*\nabla} = \bar{\mathbf{B}}, \quad (56)$$

where  $\tilde{\Pi}^{*\nabla}$  is the matrix formulation of the Ritz projection operator [31], and

$$\mathbf{M} = \int_E \hat{\boldsymbol{\varepsilon}}^T(\mathbf{m}) \hat{\mathbb{D}} \hat{\boldsymbol{\varepsilon}}(\mathbf{m}) dE, \quad \bar{\mathbf{B}} = \int_E \hat{\boldsymbol{\varepsilon}}^T(\mathbf{m}) \hat{\mathbb{D}} \hat{\boldsymbol{\varepsilon}}(\boldsymbol{\phi}) dE, \quad (57)$$

where  $\hat{\square}$  represents the Voigt form.

For  $k = 1$ , the strain matrix is

$$\hat{\boldsymbol{\varepsilon}}(\mathbf{m}) = \begin{bmatrix} \frac{\partial \mathbf{m}_1}{\partial x} & \dots & \frac{\partial \mathbf{m}_6}{\partial x} \\ \frac{\partial \mathbf{m}_1}{\partial y} & \dots & \frac{\partial \mathbf{m}_6}{\partial y} \\ \frac{\partial \mathbf{m}_1}{\partial x} + \frac{\partial \mathbf{m}_1}{\partial y} & \dots & \frac{\partial \mathbf{m}_6}{\partial x} + \frac{\partial \mathbf{m}_6}{\partial y} \end{bmatrix}. \quad (58)$$

Besides, the matrix  $\bar{\mathbf{B}}$  can be expressed using integration by parts as

$$\bar{\mathbf{B}} = \int_E \hat{\boldsymbol{\varepsilon}}^T(\mathbf{m}) \hat{\mathbb{D}} \hat{\boldsymbol{\varepsilon}}(\boldsymbol{\phi}) dE = - \int_E \left[ \nabla \cdot \left( \hat{\mathbb{D}} \hat{\boldsymbol{\varepsilon}}(\mathbf{m}) \right) \right]^T \boldsymbol{\phi} dE + \int_{\partial E} \left[ \hat{\mathbb{D}} \hat{\boldsymbol{\varepsilon}}(\mathbf{m}) \right]^T \mathbf{n} \cdot \boldsymbol{\phi} d\Gamma. \quad (59)$$

Since  $\mathbf{m} \in \mathbf{M}_k(E)$  and the divergence term involves polynomials of degree  $k - 2$ , for  $k = 1$ , the first term on the right-hand side vanishes.

The matrix  $\bar{\mathbf{D}}_{2n_v \times n_k}$  represents the evaluation of polynomial basis functions  $\mathbf{m}_\alpha$  at the degrees of freedom locations

$$\bar{\mathbf{D}}_{i\alpha} = \text{dof}_i(\mathbf{m}_\alpha), \quad i = 1, 2, \dots, 2n_v, \quad \alpha = 1, 2, \dots, n_k, \quad (60)$$

where  $\text{dof}_i(\cdot)$  denotes the  $i$ -th Dof value (nodal evaluation for the displacement field) and the dimension of the polynomial space  $\mathbf{M}_k(E)$  for  $k = 1$  is  $n_k = 6$ .

The relationship between the matrices is given by the projection system. The projection operator is determined from Eq. (56)

$$\tilde{\mathbf{\Pi}}^{*\nabla} = \mathbf{M}^{-1}\overline{\mathbf{B}} \quad (61)$$

subject to boundary constraint conditions.

For  $\mathbf{u}^h, \mathbf{v}^h \in \mathcal{V}_{\mathbf{u}}^h(E)$ , the bilinear form within an element can be decomposed as

$$a_u^E(\mathbf{u}^h, \mathbf{v}^h) = a_u^E(\mathbf{\Pi}^\nabla \mathbf{u}^h, \mathbf{\Pi}^\nabla \mathbf{v}^h) + a_u^E(\mathbf{u}^h - \mathbf{\Pi}^\nabla \mathbf{u}^h, \mathbf{v}^h - \mathbf{\Pi}^\nabla \mathbf{v}^h). \quad (62)$$

The element stiffness matrix is decomposed as

$$\mathbf{K}_{\text{VE}}^{u,E} = \mathbf{K}_E^{u,c} + \mathbf{K}_E^{u,s}, \quad (63)$$

where  $\mathbf{K}_E^{u,c}$  is the consistency part and  $\mathbf{K}_E^{u,s}$  is the stabilization part.

The consistency stiffness matrix is expressed as

$$\mathbf{K}_E^{u,c} = \left( \tilde{\mathbf{\Pi}}^{*\nabla} \right)^T \mathbf{M} \tilde{\mathbf{\Pi}}^{*\nabla}. \quad (64)$$

The stabilization stiffness matrix is expressed as [45]

$$\mathbf{K}_E^{u,s} = \tau^h \text{tr}(\mathbf{K}_E^{u,c}) \left( \mathbf{I} - \tilde{\mathbf{\Pi}}^\nabla \right)^T \left( \mathbf{I} - \tilde{\mathbf{\Pi}}^\nabla \right), \quad (65)$$

where  $\tilde{\mathbf{\Pi}}^\nabla = \overline{\mathbf{D}} \tilde{\mathbf{\Pi}}^{*\nabla}$ ,  $\tau^h$  is a stabilization parameter taken as 1/2.

Considering thermal strain, the total load vector can be expressed as

$$\mathbf{F}_{\text{VE}}^u = \mathbf{F}_{\text{ext}} + \mathbf{F}_{\text{VE}}^{th}, \quad (66)$$

where  $\mathbf{F}_{\text{ext}}$  represents the external mechanical load and  $\mathbf{F}_{\text{VE}}^{th}$  represents the global thermal load, computed as

$$\mathbf{F}_{\text{VE}}^{th} = \sum_E \left( \tilde{\mathbf{\Pi}}^{*\nabla} \right)^T \int_E \hat{\boldsymbol{\varepsilon}}^T(\mathbf{m}) \hat{\mathbb{D}} \hat{\boldsymbol{\varepsilon}}_{\text{th}} dE, \quad (67)$$

where  $\tilde{\mathbf{\Pi}}^{*\nabla}$  is the matrix formulation of the Ritz projection operator solved from Eq. (56). The thermal strain  $\hat{\boldsymbol{\varepsilon}}_{\text{th}} = \alpha(T - T_0)[1, 1, 0]^T$  is expressed in Voigt form.

### 3.3. Comparative analysis of FEM and VEM

This section presents a comparative analysis between the FEM and VEM for thermoelastic problems. The comparison examines the fundamental differences in discretization strategies, computational efficiency, and practical implementation aspects. Table 1 summarizes the key characteristics and trade-offs between these two numerical approaches across various computational and theoretical criteria.

Table 1: Key differences between FEM and VEM for thermomechanical analysis

	<b>FEM</b>	<b>VEM</b>
Mesh	Standard elements (tri/quad)	Polygonal elements of arbitrary shape
Implementation	Direct stiffness assembly	Requires projection $\Pi^\nabla$ and stabilization
Best suited for	Regular structured domains	Complex geometries with irregular interfaces
Dofs per element	Fixed (e.g., 4 for Q4)	Variable ( $n_v$ vertices)
Computational cost	More efficient for simple geometries	Additional overhead from projections

The comparative analysis reveals that FEM possesses a well-established theoretical foundation and demonstrates superior computational efficiency for regular meshes and standard geometric configurations. The method is particularly effective for standard engineering problems where the geometry can be adequately discretized using conventional element shapes. In contrast, VEM excels in handling geometrically complex problems through its ability to accommodate arbitrary polygonal elements, providing exceptional mesh flexibility and geometric adaptability. This capability is particularly valuable when dealing with irregular domains or when mesh generation becomes challenging with traditional finite elements.

To leverage the complementary strengths highlighted in Table 1, this study proposes a FE-VE coupling approach that strategically combines both methods. The coupling strategy assigns FEM to regular regions where computational efficiency is paramount, while utilizing VEM in geometrically complex areas where mesh flexibility is essential. This hybrid approach aims to achieve optimal computational efficiency while maintaining solution accuracy for multi-scale geometric structures encountered in electronic packaging applications.

#### 4. FE-VE coupling strategy

This section presents a comprehensive FE-VE coupling strategy specifically designed to address geometric multi-scale challenges in electronic packaging applications. The methodology strategically combines the computational efficiency of finite elements with the geometric flexibility of virtual elements through systematic domain decomposition and robust interface treatment. The coupling approach is based on three key components: (i) domain partitioning criteria that identify regions suitable for each method, (ii) interface compatibility conditions that ensure continuity across FE-VE boundaries, and (iii) solution transfer mechanisms that maintain accuracy during the coupling process. The strategy aims to optimize computational resources while preserving solution quality for complex geometries encountered in modern electronic systems.

##### 4.1. Domain decomposition

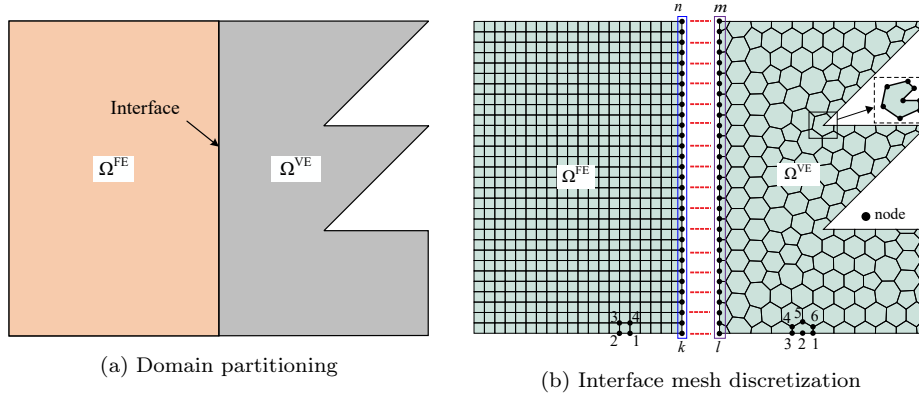


Figure 2: FE-VE coupling approach. (a) The computational domain is partitioned into finite element and virtual element regions based on geometric complexity. (b) The interface mesh discretization ensures compatibility between FE and VE domains through coincident nodes along the coupling boundary.

As illustrated in Fig. 2a, the computational domain  $\Omega$  is partitioned into two complementary regions based on geometric complexity: the finite element domain  $\Omega^{\text{FE}}$  and the virtual element domain  $\Omega^{\text{VE}}$ , such that  $\Omega = \Omega^{\text{FE}} \cup \Omega^{\text{VE}}$  with  $\Omega^{\text{FE}} \cap \Omega^{\text{VE}} = \emptyset$ . The FEM is deployed in  $\Omega^{\text{FE}}$  to efficiently handle regular geometric regions with structured quadrilateral meshes, while the VEM is employed in  $\Omega^{\text{VE}}$  to accommodate complex geometric configurations using arbitrary polygonal elements.

The coupling between the two domains is achieved through interface treatment at the shared boundary  $\Gamma^{\text{inter}} = \partial\Omega^{\text{FE}} \cap \partial\Omega^{\text{VE}}$ . Fig. 2b demonstrates the discretization strategy, where the finite element region utilizes a regular quadrilateral mesh while the virtual element region employs polygonal elements that conform to the complex geometric boundaries. The interface compatibility is established through coincident nodes along  $\Gamma^{\text{inter}}$ , where finite element boundary nodes and their corresponding virtual element boundary nodes share identical spatial coordinates. This nodal correspondence ensures displacement continuity across the coupling boundary, expressed as

$$\mathbf{u}^{\text{FE}}|_{\Gamma^{\text{inter}}} = \mathbf{u}^{\text{VE}}|_{\Gamma^{\text{inter}}}. \quad (68)$$

As shown in Fig. 2b, the interface nodes are strategically positioned to ensure compatibility along the coupling boundary. The figure illustrates typical element configurations: a four-node finite element (numbered 1, 2, 3, 4) in the structured quadrilateral mesh region and a six-node virtual element (numbered 1, 2, 3, 4, 5, 6) in the polygonal mesh region. The actual interface nodes are indexed from  $k$  to  $n$  on the finite element side and from  $l$  to  $m$  on the virtual element side, where coincident nodal positioning ensures displacement continuity across the FE-VE boundary.

#### 4.2. Interface treatment

The coupling between finite element and virtual element domains requires systematic treatment of interface variables to ensure displacement continuity and force equilibrium. This section presents the partitioning strategy and assembly procedure for establishing the coupled system.

##### 4.2.1. Matrix partitioning for interface treatment

Both finite element and virtual element domains are partitioned to separate interior and interface Dofs based on the nodal positions illustrated in Fig. 2b.

*Finite element domain.* The finite element system is partitioned into block matrix form

$$\begin{bmatrix} \mathbf{K}_{FF} & \mathbf{K}_{FI} \\ \mathbf{K}_{IF} & \mathbf{K}_{II}^{\text{FE}} \end{bmatrix} \begin{Bmatrix} \mathbf{u}_F \\ \mathbf{u}_I^{\text{FE}} \end{Bmatrix} = \begin{Bmatrix} \mathbf{F}_F \\ \mathbf{F}_I^{\text{FE}} \end{Bmatrix}, \quad (69)$$

where  $\mathbf{u}_I^{\text{FE}} = [u_k, u_{k+1}, \dots, u_n]^T$  represents the displacement variables at interface nodes (nodes  $k$  to  $n$  in Fig. 2b),  $\mathbf{u}_F$  represents interior node displacements, and  $\mathbf{K}_{II}^{\text{FE}}$  is the interface stiffness contribution from the finite element domain.

*Virtual element domain.* Similarly, the virtual element system is partitioned as

$$\begin{bmatrix} \mathbf{K}_{VV} & \mathbf{K}_{VI} \\ \mathbf{K}_{IV} & \mathbf{K}_{II}^{\text{VE}} \end{bmatrix} \begin{Bmatrix} \mathbf{u}_V \\ \mathbf{u}_I^{\text{VE}} \end{Bmatrix} = \begin{Bmatrix} \mathbf{F}_V \\ \mathbf{F}_I^{\text{VE}} \end{Bmatrix}, \quad (70)$$

where  $\mathbf{u}_I^{\text{VE}} = [u_l, u_{l+1}, \dots, u_m]^T$  represents interface node displacements (nodes  $l$  to  $m$  in Fig. 2b),  $\mathbf{u}_V$  represents interior virtual element nodes, and  $\mathbf{K}_{II}^{\text{VE}}$  is the interface stiffness contribution from the virtual element domain.

#### 4.2.2. Strong coupling implementation

At the FE-VE interface, a strong coupling scheme is employed where corresponding nodes are matched to ensure displacement compatibility

$$\mathbf{u}_I^{\text{FE}} = \mathbf{u}_I^{\text{VE}} = \mathbf{u}_I. \quad (71)$$

The strong coupling implementation follows a systematic assembly procedure. As established in Eqs. (69) and (70), the finite element and virtual element systems are constructed independently in their respective domains with appropriate partitioning for interior and interface degrees of freedom.

Due to the displacement compatibility condition at the interface (Eq. (71)), the interface degrees of freedom are unified. The coupling is achieved by recognizing that interface nodes belong simultaneously to both domains, and their stiffness and load contributions must be properly combined. By assembling the partitioned systems from Eqs. (69) and (70), a coupled global system is obtained

$$\begin{bmatrix} \mathbf{K}_{FF} & \mathbf{K}_{FI} & \mathbf{0} \\ \mathbf{K}_{IF} & \mathbf{K}_{II}^{\text{FE}} + \mathbf{K}_{II}^{\text{VE}} & \mathbf{K}_{IV} \\ \mathbf{0} & \mathbf{K}_{VI} & \mathbf{K}_{VV} \end{bmatrix} \begin{Bmatrix} \mathbf{u}_F \\ \mathbf{u}_I \\ \mathbf{u}_V \end{Bmatrix} = \begin{Bmatrix} \mathbf{F}_F \\ \mathbf{F}_I^{\text{FE}} + \mathbf{F}_I^{\text{VE}} \\ \mathbf{F}_V \end{Bmatrix}, \quad (72)$$

where subscripts  $F$ ,  $I$ , and  $V$  denote finite element interior nodes, interface nodes, and virtual element interior nodes, respectively. The key features of this coupling formulation are (i) The off-diagonal blocks  $\mathbf{K}_{FI}$  and  $\mathbf{K}_{IF}$  represent the coupling between FE interior nodes and interface nodes, arising from finite elements adjacent to the interface. (ii) Similarly,  $\mathbf{K}_{IV}$  and  $\mathbf{K}_{VI}$  represent the coupling between interface nodes and VE interior nodes from virtual elements adjacent to the interface. (iii) The diagonal interface block  $\mathbf{K}_{II}^{\text{FE}} + \mathbf{K}_{II}^{\text{VE}}$  represents the additive stiffness contributions from both domains. This linear superposition is mathematically valid because both

methods discretize the same underlying continuum problem, and the interface nodes serve as connection points where element-level contributions are naturally summed during standard assembly procedures. (iv) The interface load vector  $\mathbf{F}_I^{\text{FE}} + \mathbf{F}_I^{\text{VE}}$  combines load contributions from both domains, including external mechanical loads and thermal expansion effects, ensuring proper load transfer across the coupling boundary. (v) The zero blocks in the upper-right and lower-left corners reflect the absence of direct coupling between FE and VE interior nodes, as these nodes interact only through the shared interface.

This strong coupling approach ensures that both displacement continuity and traction equilibrium are satisfied at the interface, maintaining the physical consistency of the coupled solution. The resulting system can be solved using standard sparse linear solvers, with the coupling naturally handled through the unified interface degrees of freedom.

#### *4.3. Implementation workflow*

The comprehensive implementation workflow for the FE-VE coupled thermomechanical analysis is illustrated in Fig. 3, demonstrating the seamless integration of preprocessing, analysis, and post-processing phases. The computational procedure follows a systematic three-stage approach.

##### *4.3.1. Pre-processing stage*

The preprocessing phase establishes the computational framework through strategic domain partitioning and mesh generation. The geometry is initially defined and systematically partitioned into FE and VE domains based on geometric complexity considerations. The FE domain  $\Omega^{\text{FE}}$  employs structured quadrilateral elements to efficiently handle regular geometric regions, while the VE domain  $\Omega^{\text{VE}}$  utilizes arbitrary polygonal elements to accommodate complex geometric configurations.

The mesh generation process discretizes each domain using appropriate element types and establishes proper nodal connectivity at the FE-VE interface. This stage ensures geometric compatibility between the two domains and prepares the foundation for the subsequent coupling implementation detailed in Sec. 4.2.

##### *4.3.2. Thermal analysis phase*

The thermal analysis phase implements the heat conduction formulation established in Sec. 2.2. For the FE domain, standard shape functions are

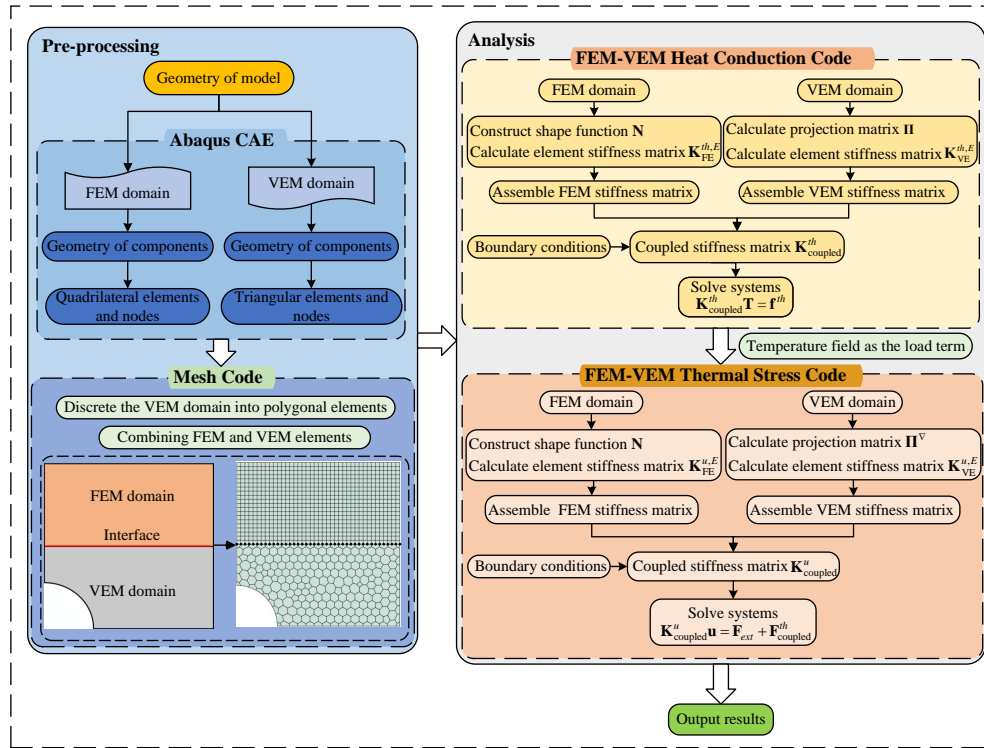


Figure 3: Thermomechanical coupling analysis based on FE-VE coupled method.



constructed and element thermal stiffness matrices  $\mathbf{K}_{\text{FE}}^{th,E}$  are computed using the procedures described in Sec. 3.1.1. Simultaneously, the VE domain employs projection operators to calculate element stiffness matrices  $\mathbf{K}_{\text{VE}}^{th,E}$  following the VEM formulation.

The individual domain contributions are assembled into the coupled global thermal stiffness matrix  $\mathbf{K}_{\text{coupled}}^{th}$  according to the interface treatment methodology. After applying appropriate thermal boundary conditions, the coupled thermal system

$$\mathbf{K}_{\text{coupled}}^{th} \mathbf{T} = \mathbf{f}_{\text{coupled}}^{th} \quad (73)$$

is solved to obtain the temperature distribution  $\mathbf{T}$  throughout the computational domain.

#### 4.3.3. Thermoelastic analysis phase

The mechanical analysis phase utilizes the computed temperature field as thermal loading input, implementing the thermomechanical coupling described in Sec. 2.2. Following procedures analogous to the thermal analysis, shape functions are constructed and element mechanical stiffness matrices are computed for both domains:  $\mathbf{K}_{\text{FE}}^{u,E}$  for the finite element region and  $\mathbf{K}_{\text{VE}}^{u,E}$  for the virtual element region.

The thermal load vector  $\mathbf{F}_{\text{coupled}}^{th}$  is computed based on the temperature field obtained from the thermal analysis, incorporating thermal expansion effects. After assembling the coupled global mechanical stiffness matrix and applying appropriate displacement boundary conditions, the coupled mechanical system

$$\mathbf{K}_{\text{coupled}}^u \mathbf{u} = \mathbf{F}_{\text{ext}} + \mathbf{F}_{\text{coupled}}^{th} \quad (74)$$

is solved to obtain the displacement field  $\mathbf{u}$  and subsequently the stress distribution throughout the domain.

#### 4.3.4. Post-processing and output

The final stage involves post-processing to extract engineering quantities of interest. Stress fields are computed using the established constitutive relationships, and von Mises equivalent stresses are evaluated for reliability assessment. The workflow concludes with the generation of visualization outputs including temperature distributions, displacement fields, and stress contours, providing insight into the thermomechanical behavior of the analyzed system.

## 5. Numerical Examples

### 5.1. Square plate with circular hole

To demonstrate the computational efficiency and convergence characteristics of the proposed algorithm, a square plate with a circular hole subjected to uniform loading is presented as the first numerical example. Due to the symmetric nature of the model, only one quarter of the domain is analyzed by exploiting symmetry conditions, as illustrated in Fig. 4. The model parameters are specified as follows: circular hole radius  $r = 5$  mm, plate dimension  $a = 20$  mm, applied load intensity  $F = 5$  MPa, elastic modulus  $E = 10$  MPa, and Poisson's ratio  $\nu = 0.3$ . The problem is solved under plane stress conditions.

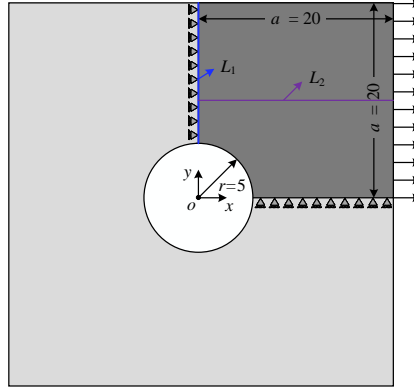


Figure 4: Geometric configuration and boundary conditions.

Three different numerical approaches were employed to solve this problem: VEM, FEM, and the proposed FE-VE coupling method. The domain is partitioned such that the regular regions employ finite elements while the area near the circular hole utilizes virtual elements to handle the geometric complexity. The resulting von Mises stress distribution contours are presented in Fig. 5. The stress contours demonstrate excellent agreement among all three methods, particularly around the critical stress concentration region near the circular hole. Fig. 5(a) shows the VEM solution with its characteristic polygonal mesh that naturally adapts to the curved boundary geometry. Fig. 5(b) presents the FEM solution employing a structured quadrilateral mesh, while Fig. 5(c) illustrates the FE-VE coupling approach that effectively combines the advantages of both methods. The stress magnitude distributions and

overall stress patterns are highly consistent across all three approaches, confirming the accuracy and reliability of the proposed coupling methodology.

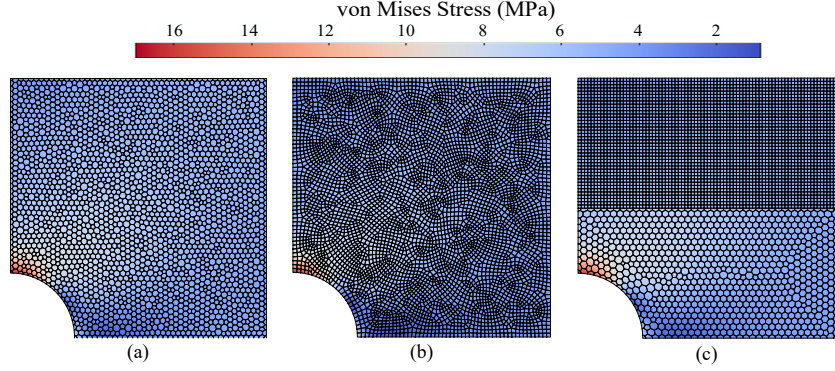


Figure 5: von Mises stress distribution comparison for square plate with circular hole: (a) VEM solution, (b) FEM solution, (c) FE-VE coupling solution.

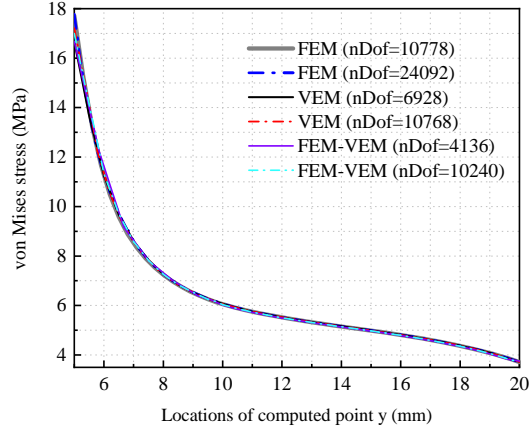


Figure 6: Stress distribution along line  $L_1$  for different methods with varying nDofs.

The stress distributions along the line  $L_1$  (given in Fig. 4) were extracted for FEM, VEM, and FE-VE method under different Dofs, as illustrated in Fig. 6. The results demonstrate excellent agreement among all three approaches, confirming the accuracy and consistency of the proposed coupling methodology. Additionally, the computational times for the three methods were compared, as presented in Table 2. From Table 2, it is evident that computational time increases with the number of degrees of freedom (nDofs)

for all three methods, which is expected behavior. When comparing methods with similar Dof (approximately 10,700), VEM demonstrates slightly better computational efficiency than FEM, requiring 2.06 seconds compared to 2.4 seconds for FEM. This efficiency gain is primarily attributed to VEM’s ability to achieve comparable accuracy using fewer elements (2,595 vs 5,263), thereby reducing the computational overhead. The FE-VE coupling approach shows competitive performance, with computational times that fall between pure VEM and pure FEM solutions, while providing the geometric flexibility advantages of the hybrid approach.

Table 2: Computational time comparison for VEM, FEM, and FE-VE coupled method.

Method	Number of elements	nDof	Time (s)
VEM	1655	6928	1.25
	2595	10768	2.06
FEM	5263	10778	2.4
	11850	24092	7.29
FEM-VEM	1611	4136	1.11
	4083	10240	3.05

To investigate the convergence characteristics of the FE-VE algorithm, calculations were performed using meshes of varying densities. The coupling interface along the line  $L_2$  (shown in Fig. 4) was selected as the computational output and comparison path for detailed analysis. The mean relative error (MRE) is defined as

$$\text{MRE} = \frac{1}{N} \sum_{n=1}^N \left| \frac{\sigma_{\text{num}} - \sigma_{\text{ref}}}{\sigma_{\text{ref}}} \right|, \quad (75)$$

where  $N$  represents the total number of nodes in the calculation,  $\sigma_{\text{num}}$  denotes the numerical solution of nodal stress, and  $\sigma_{\text{ref}}$  represents the reference solution of nodal stress.

Fig. 7 presents the MRE convergence comparison for FEM, VEM, and FE-VE coupling method as the nDof increases from approximately 5,000 to 25,000. The convergence analysis reveals distinct performance characteristics for each method, with convergence rates indicated by the slope annotations in the figure. FEM demonstrates the fastest convergence with a rate of 0.43, showing the steepest error reduction from approximately  $1.3 \times 10^{-3}$  to  $6.2 \times 10^{-4}$ . VEM exhibits a convergence rate of 0.338, with errors decreasing

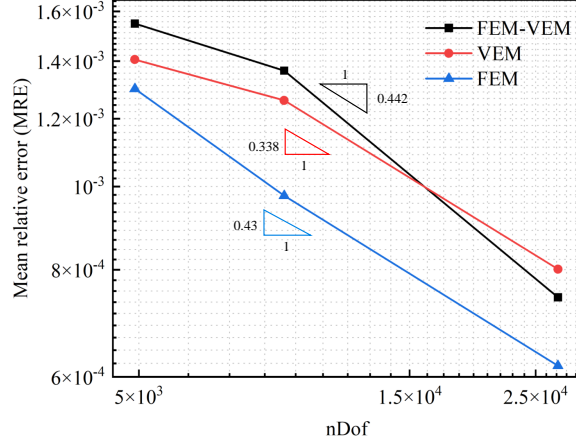


Figure 7: Convergence analysis: MRE comparison of different numerical algorithm.

from  $1.41 \times 10^{-3}$  to  $8.0 \times 10^{-4}$ , demonstrating consistent performance across the degree-of-freedom range. The FE-VE coupling method achieves a convergence rate of 0.442, reducing errors from  $1.56 \times 10^{-3}$  to  $7.3 \times 10^{-4}$ , performing competitively with pure FEM. The convergence rates indicate that the FE-VE coupling method actually achieves slightly better convergence behavior than pure FEM, while VEM shows the most gradual convergence. All three methods demonstrate stable convergence trends, confirming the reliability of the proposed coupling strategy. The FE-VE approach maintains good accuracy while providing the additional advantage of geometric flexibility for complex domain geometries.

### 5.2. Thermoelastic analysis of thick-walled cylindrical structure

We analyze a homogeneous thick-walled cylinder under thermal loading to validate the FEM-VEM coupling method. The analytical solution for this problem serves as a benchmark for accuracy assessment. Fig. 8 illustrates the geometry and boundary conditions of this verification case.

The cylinder has inner radius  $r_a = 20$  mm and outer radius  $r_b = 60$  mm. Material properties include Young's modulus  $E = 460000$  MPa, Poisson's ratio  $\nu = 0.3$ , thermal expansion coefficient  $\alpha = 7.4 \times 10^{-6}$  K $^{-1}$ , and thermal conductivity  $\lambda = 20$  W/(m·K). The thermal boundary conditions consist of  $T_a = 0$  K at the inner surface and  $T_b = 500$  K at the outer surface under steady-state conditions. Due to symmetry, only one quarter of the cylinder is modeled to optimize computational efficiency, as shown in Fig. 8.

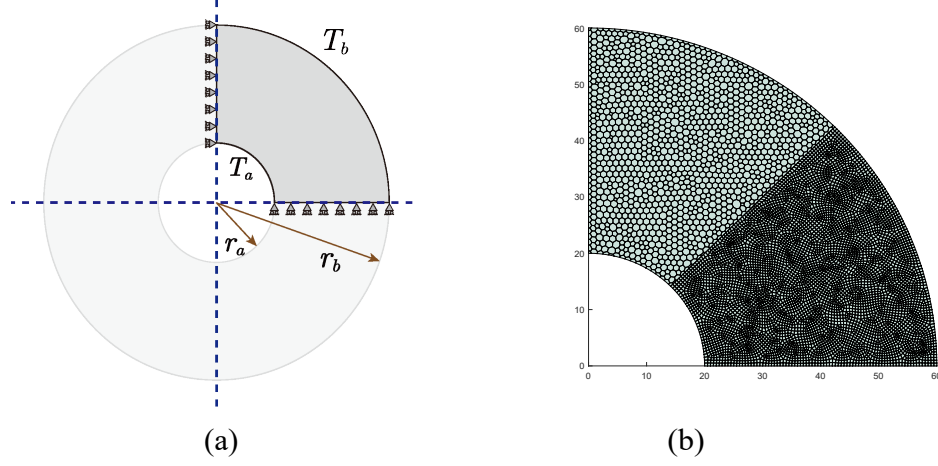


Figure 8: Thick-walled cylinder configuration: (a) Full geometry with inner radius  $r_a$ , outer radius  $r_b$ , and applied temperatures  $T_a$  and  $T_b$ ; (b) Mesh employed in the FEM-VEM coupled method

Given the material parameters and boundary conditions, the analytical temperature field is

$$T = T_a + \frac{T_b - T_a}{\ln(r_b/r_a)} \ln\left(\frac{r}{r_a}\right), \quad (76)$$

where  $r$  represents the radial coordinate.

The method's convergence characteristics are assessed using the root mean square (RMS)  $L^2$  error as the accuracy metric. This normalized error measure is defined as

$$\varepsilon_{\text{rms}} = \frac{1}{\max(|X_e|)} \sqrt{\frac{1}{N} \sum_{i=1}^N |X - X_e|^2} \quad (77)$$

where  $N$  is the number of evaluation points, and  $X_e$  and  $X$  denote the analytical and numerical solutions, respectively.

Fig. 9 presents the convergence analysis comparing FEM-VEM coupling, pure VEM, and pure FEM methods, showing RMS errors for temperature as functions of degrees of freedom. The convergence rates, indicated by the slope annotations in the figure, demonstrate that the VEM achieves a convergence rate of 1.02, while the FEM-VEM coupling method exhibits a rate of

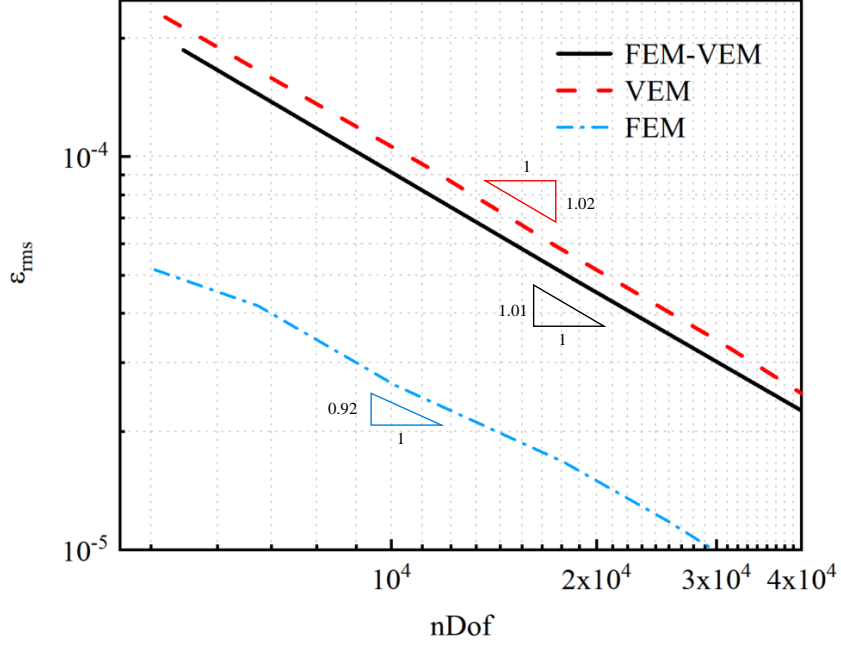


Figure 9: Temperature accuracy versus mesh refinement for thick-walled cylinder

1.01, both outperforming pure FEM with a rate of 0.92. The proposed FEM-VEM coupling method maintains nearly optimal convergence characteristics comparable to pure VEM, while providing the additional advantage of geometric flexibility through strategic domain partitioning. All three methods show consistent error reduction with mesh refinement, confirming the stability and reliability of the coupling approach.

### 5.3. Simplified sintered silver model

The third numerical example investigates a sintered silver interconnect structure commonly employed in high-power electronic packaging applications. As illustrated in Fig. 10, the model adopts a typical ‘sandwich’ configuration consisting of three distinct layers: a SiC chip (top), sintered silver interconnect layer (middle), and copper substrate (bottom). This multi-layer structure is representative of modern power electronic modules where effective thermal management and mechanical reliability are critical design considerations [8]. The geometric dimensions are specified as follows: the SiC chip has width  $b = 1.8$  mm and thickness  $h_1 = 0.5$  mm; the sintered silver layer maintains the same width as the SiC chip with thickness  $h_2 = 0.3$  mm;

and the copper substrate has width  $a = 3$  mm and thickness  $h_3 = 0.8$  mm. The material properties for each component are detailed in Table 3, which reveal significant differences in thermal and mechanical characteristics that contribute to complex thermomechanical stress development during thermal loading.

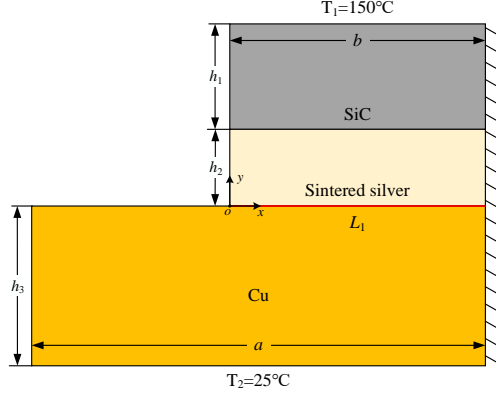


Figure 10: Geometric configuration and thermal boundary conditions.

Table 3: Material properties of sintered silver interconnect model components.

Material	Young's modulus (GPa)	Poisson's ratio	Thermal conductivity (W/m·K)	CTE $\alpha$ ( $^{\circ}\text{C}^{-1}$ )
SiC chip	410	0.14	370	$4.5 \times 10^{-6}$
Sintered silver	12.9	0.38	278	$19.0 \times 10^{-6}$
Copper substrate	110	0.38	400	$16.5 \times 10^{-6}$

The top surface is subjected to a temperature of  $T_1 = 150$   $^{\circ}\text{C}$  representing heat generation from the semiconductor device, while the bottom surface is maintained at ambient temperature  $T_2 = 25$   $^{\circ}\text{C}$ . All lateral surfaces are treated as thermally insulated. Mechanically, the right edge is fully constrained ( $u_x = u_y = 0$ ). To demonstrate the capabilities of the FE-VE coupling approach, the upper layers (SiC chip and sintered silver) are discretized using virtual elements, while the copper substrate employs conventional finite elements.

For the numerical computation, the model is discretized using Abaqus preprocessing capabilities combined with custom MATLAB code, where the virtual element domain (upper layers) employs polygonal mesh elements to leverage VEM's geometric flexibility, while the finite element domain (copper



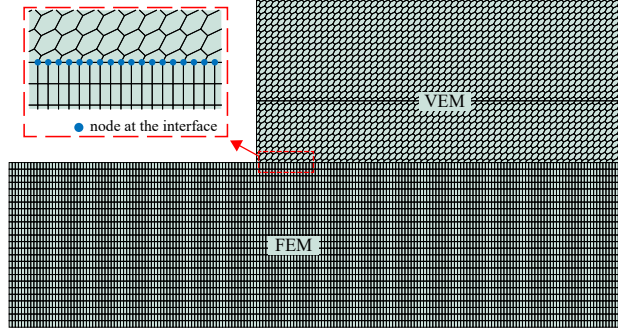


Figure 11: Hybrid mesh discretization strategy for FEM-VEM coupling analysis.

substrate) utilizes conventional four-node quadrilateral elements for computational efficiency. A critical aspect of the implementation is ensuring nodal compatibility at the coupling interface, where nodes from both domains must be properly matched to maintain solution continuity, as illustrated in Fig. 11. The figure demonstrates the distinct meshing approaches for each domain and the interface treatment, where polygonal elements transition to structured quadrilateral elements while maintaining nodal correspondence. This interface treatment ensures that displacement and stress continuity conditions are satisfied across the domain boundary, which is essential for the accuracy and stability of the FE-VE coupling scheme.

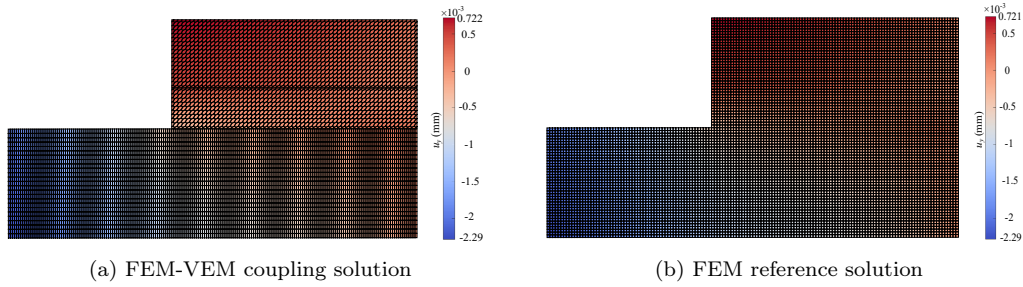


Figure 12: Comparison of displacement ( $u_y$ ) distributions.

The computational accuracy of the FE-VE coupling algorithm is validated through comparison with a refined finite element solution. Fig. 12 presents the overall displacement ( $u_y$ ) contours, demonstrating that both methods yield very similar results across the entire domain. The displacement patterns exhibit expected thermal expansion behavior, with upper layers (SiC and sintered silver) experiencing upward displacement due to thermal loading

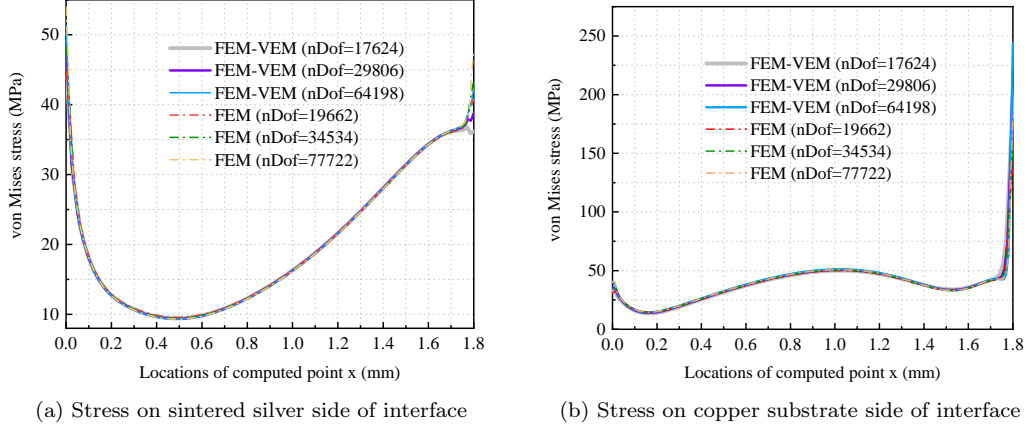


Figure 13: Stress distributions along both sides of coupling interface  $L_1$  (shown in Fig. 10).

while the constrained right boundary maintains zero displacement.

To provide detailed accuracy assessment, von Mises stress values at each node along coupling interface line  $L_1$  (given in Fig. 10) were extracted for both sintered silver and copper substrate layers, as shown in Fig. 13. The comparison reveals good agreement between the FE-VE coupling algorithm and the reference solution across different mesh refinement levels, with stress distributions showing consistent convergence trends. The stress profiles demonstrate expected material-dependent behavior, with peak stresses reaching approximately 50 MPa at the sintered silver interface and up to 260 MPa at the copper substrate interface. The significantly higher stresses in the copper substrate can be attributed to its higher elastic modulus (110 GPa vs 12.9 GPa for sintered silver), which results in greater stress concentrations under thermal loading conditions. These results confirm the capability of the proposed coupling methodology to accurately capture critical stress distributions in multi-material electronic packaging applications.

Previous analyses examined the thermomechanical behavior of sintered silver structures with flat interfaces. However, in practical applications, interface morphology often exhibits complex geometric characteristics such as random roughness rather than ideal smoothness. This geometric complexity can induce significant local stress concentrations and alter load transfer paths within the structure, thereby critically influencing overall mechanical performance. To more accurately predict the mechanical response of such structures, we establish and analyze a simplified model with a randomly complex-shaped interface, whose geometric configuration is shown in Fig. 14.

The model has geometric parameters  $a = 40$  mm and  $b = 20$  mm and consists of three distinct parts with material properties listed in Table 4. Temperature boundary conditions are applied at the top surface ( $T_1 = 150$  °C) and bottom surface ( $T_0 = 25$  °C), with all other surfaces thermally insulated. The bottom surface is subjected to a fully fixed mechanical constraint.

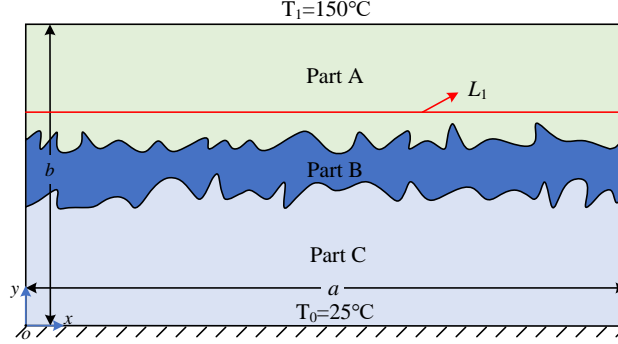


Figure 14: Simplified model with complex-shaped interface featuring three material regions (Parts A, B, C) and irregular interface geometry.

Table 4: Material properties of Complex interface model components.

Material	Young's modulus (GPa)	Poisson's ratio	Thermal conductivity (W/m·K)	CTE $\alpha$ ( $^{\circ}\text{C}^{-1}$ )
Part A	69.5	0.33	234	$23.2 \times 10^{-6}$
Part B	1.2	0.47	3.2	$92 \times 10^{-6}$
Part C	187	0.28	147	$2.6 \times 10^{-6}$

To demonstrate the advantages of the FE-VE method in handling complex geometries, a coupled analysis is performed where the virtual element method discretizes regions around the complex interface while the FEM is applied to regular regions. The finite element domain employs four-node quadrilateral elements, whereas the virtual element domain utilizes arbitrary polygonal elements that flexibly conform to the irregular interface geometry. The corresponding mesh discretization is illustrated in Fig. 15.

To validate the computational accuracy of the FE-VE method, results are compared with a refined pure finite element analysis. Fig. 16 presents the displacement and von Mises stress distributions in Part B near the complex interface, revealing excellent agreement between both methods. Both approaches accurately capture the stress concentration phenomena at the

irregular interface, thereby verifying the effectiveness and reliability of the FE-VE method for modeling structures with complex geometries.

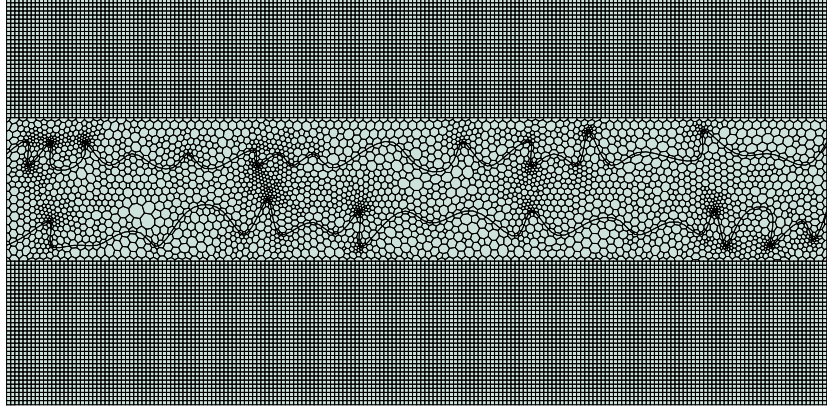


Figure 15: Hybrid mesh discretization strategy for the model with complex interface: quadrilateral elements in regular regions and polygonal elements near irregular interface

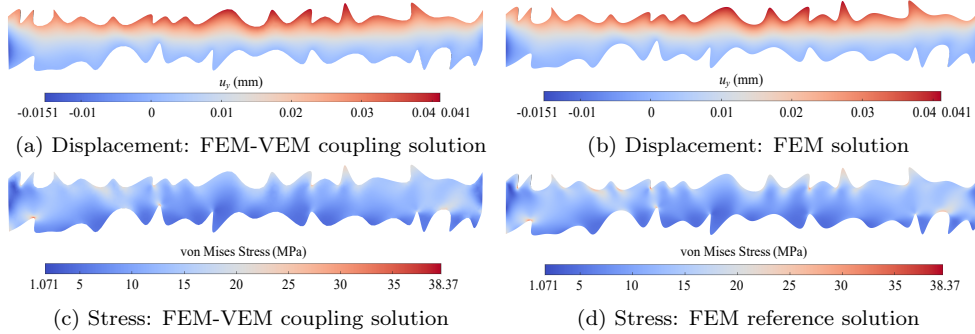


Figure 16: Comparison of displacement and von Mises stress distributions in Part B.

To quantitatively assess the coupling accuracy, displacement and stress distributions along the interface line  $L_1$  (shown in Fig. 14) are extracted and compared with the refined FEM reference solution ( $nDof = 165,982$ ). Fig. 17a shows that the horizontal displacement peaks near the midpoint at approximately 0.045 mm. Fig. 17b reveals a nearly linear vertical displacement distribution ranging from  $-0.065$  mm to  $0.065$  mm. Fig. 17c demonstrates that the von Mises stress exhibits significant fluctuations between 4 MPa and 23 MPa due to the complex interface geometry.

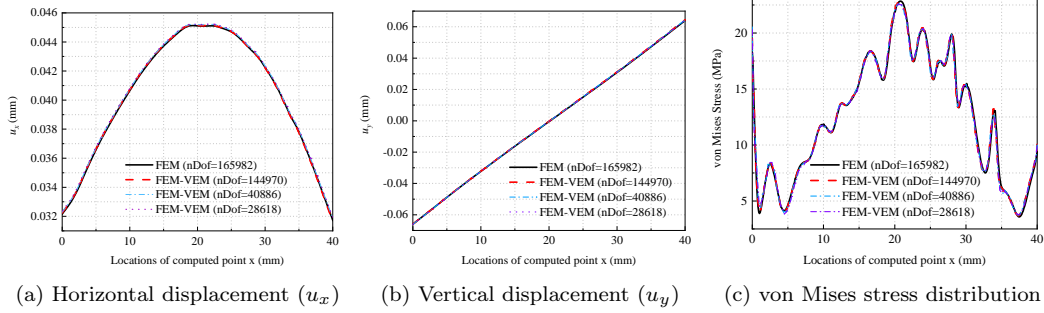


Figure 17: Displacement and stress distributions along coupling interface line  $L_1$ .

The FE-VE solutions show excellent agreement with the FEM reference across all three mesh densities. As the mesh is refined, the coupled method results converge systematically toward the reference solution, demonstrating good accuracy and convergence characteristics for problems involving complex geometries.

#### 5.4. FC-BGA Model

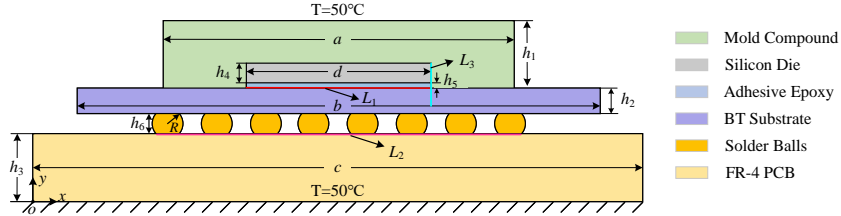


Figure 18: Geometric configuration and component layout of FC-BGA model.

Table 5: Geometric dimensions of FC-BGA module components (mm).

Component	Length	Thickness
Mold Compound	$a = 9.00$	$h_1 = 1.20$
BT Substrate	$b = 11.00$	$h_2 = 0.40$
FR-4 PCB	$c = 13.50$	$h_3 = 0.80$
Silicon Die	$d = 5.00$	$h_4 = 0.30$
Adhesive Epoxy	$d = 5.00$	$h_5 = 0.10$
Solder Balls	$R = 0.76$	$h_6 = 0.56$

The fourth numerical example examines the thermomechanical performance of a Flip-Chip Ball Grid Array (FC-BGA) packaging structure under

thermal loading conditions. FC-BGA packaging technology offers advantages of high integration density and superior performance with excellent product reliability and stability, making it widely adopted in high-performance processors and advanced semiconductor devices. As illustrated in Fig. 18, the computational model consists of six distinct components: mold compound, silicon die, adhesive epoxy, BT substrate, solder balls, and FR-4 PCB. The geometric dimensions of each component are detailed in Table 5.

Table 6: Material properties of FC-BGA model components.

Material	Young's modulus (GPa)	Poisson's ratio	Thermal conductivity (W/m·K)	CTE $\alpha$ ( $^{\circ}\text{C}^{-1}$ )
Mold Compound	24	0.25	2.1	$10 \times 10^{-6}$
Silicon Die	165.5	0.25	119	$2.8 \times 10^{-6}$
Solder Balls	11	0.11	73	$35 \times 10^{-6}$
Adhesive Epoxy	2.6	0.3	0.188	$90 \times 10^{-6}$
BT Substrate	26	0.19	14.5	$14 \times 10^{-6}$
FR-4 PCB	22	0.28	6.5	$18 \times 10^{-6}$

The material properties detailed in Table 6 show significant variations in thermal and mechanical characteristics that contribute to complex thermomechanical interactions. The boundary conditions are defined as follows: the bottom surface is fully constrained, the silicon die temperature is set to  $T = 500^{\circ}\text{C}$ , the upper surface of the mold compound and lower surface of the FR-4 PCB are maintained at the given temperature  $T = 50^{\circ}\text{C}$ , and all remaining surfaces are treated as thermally insulated. This configuration creates a severe thermal gradient across the package with substantial thermal expansion mismatches ranging from  $2.8 \times 10^{-6}^{\circ}\text{C}^{-1}$  for silicon to  $90 \times 10^{-6}^{\circ}\text{C}^{-1}$  for adhesive epoxy, generating significant thermomechanical stresses that make this an excellent test case for evaluating the FE-VE coupling methodology in complex multi-material electronic packaging applications where reliability assessment is critical.

In this numerical example, the regular geometrical regions consisting of the BT substrate and FR-4 PCB are discretized using the finite element domain, while the remaining components are assigned to the virtual element domain. The finite element domain employs four-node quadrilateral elements for discretization, while the virtual element domain utilizes regular polygonal elements at interface boundaries and arbitrary polygonal elements in non-interface regions, with non-conforming mesh techniques used to integrate the VEM domain meshes into a unified structure. To ensure

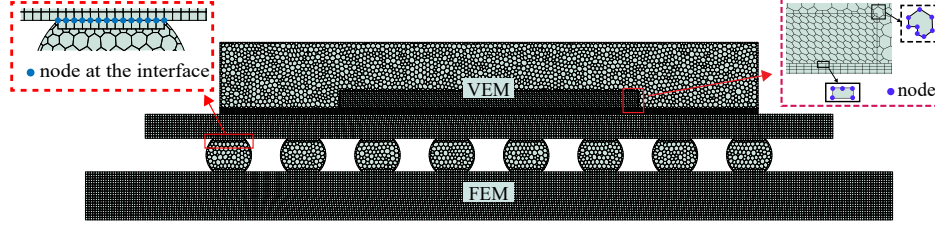


Figure 19: Hybrid mesh discretization strategy for FC-BGA model.

nodal compatibility at the coupling interface, careful attention is given to maintaining nodal correspondence between domains. Fig. 19 illustrates the final mesh discretization scheme, demonstrating the hybrid meshing strategy where complex geometries of the upper package components (mold compound, silicon die, adhesive epoxy) and solder balls are effectively handled by the flexible VEM approach, while structured lower layers benefit from the computational efficiency of conventional FEM. The interface region clearly shows how nodal correspondence between VE and FE domains is maintained to ensure solution continuity across the coupling boundary, demonstrating the seamless integration of both numerical methods in this complex multi-material electronic packaging configuration.

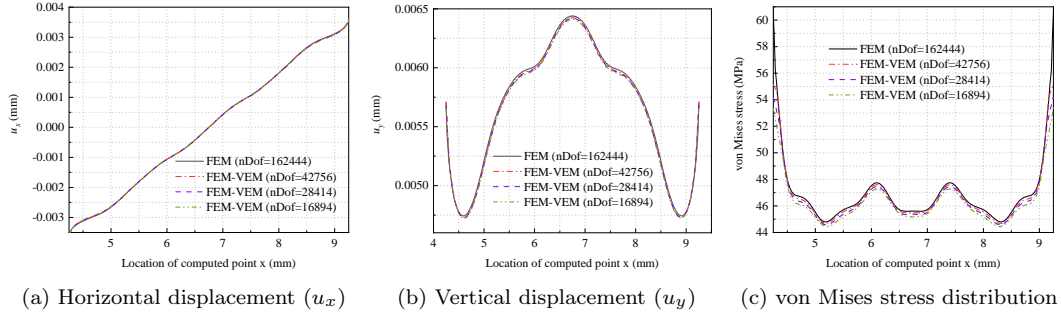


Figure 20: Displacement and stress distributions along interface line  $L_1$ .

To further validate the computational accuracy of the FE-VE coupling algorithm, a refined finite element analysis with mesh densification (nDof = 162,444) was performed as the reference solution. The displacement and stress profiles were extracted along two critical lines  $L_1$  and  $L_2$  (given in Fig. 18), as presented in Figs. 20 and 21. Fig. 20 demonstrates excellent agreement between the coupling algorithm and the reference FEM solution across all three response quantities along interface  $L_1$ . Fig. 20a shows the



horizontal displacement exhibiting a nearly linear variation from approximately -0.003 mm to 0.004 mm, indicating consistent thermal expansion behavior with virtually identical results across all mesh refinement levels. Fig. 20b presents the vertical displacement distribution with a characteristic bell-shaped profile peaking at approximately 0.0065 mm at the interface center, corresponding to maximum thermal expansion due to the temperature gradient across package layers. Fig. 20c illustrates the stress distribution with periodic variations, showing peak stresses of approximately 60 MPa at interface boundaries and local minima of 44-46 MPa in central regions.

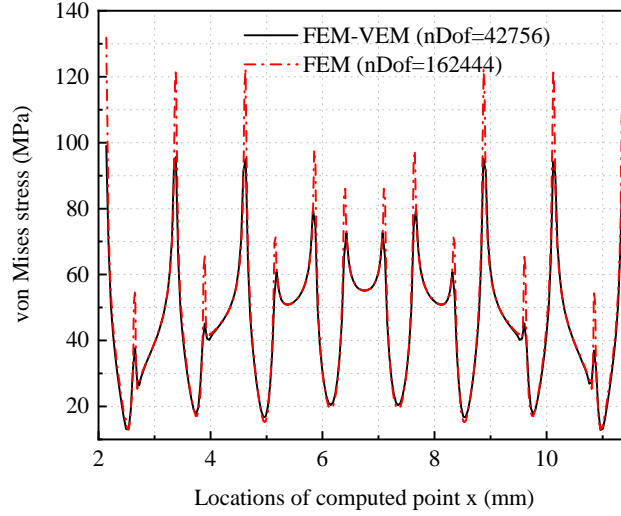


Figure 21: von Mises stress distribution along line  $L_2$ .

Fig. 21 presents the von Mises stress distribution along line  $L_2$  (shown in Fig. 18), which passes through the solder ball array. The stress profile exhibits pronounced periodic variations corresponding to the solder ball locations, with peak stresses reaching approximately 130 MPa at the solder ball interfaces and decreasing to about 20 MPa in the substrate regions between balls. The comparison between FE-VE coupling (nDof = 42,756) and reference FEM solution (nDof = 162,444) shows reasonable agreement in capturing the periodic stress pattern, though some differences are observed at stress concentration locations due to the coarser discretization in the coupling method. Despite the lower mesh density, the FE-VE approach successfully captures the overall stress distribution characteristics and solder ball interface behavior.



These comprehensive results demonstrate that the FE-VE coupling algorithm maintains computational accuracy in both regular and complex geometrical regions, effectively combining the computational efficiency of finite elements with the geometric flexibility of virtual elements for multi-scale electronic packaging applications.

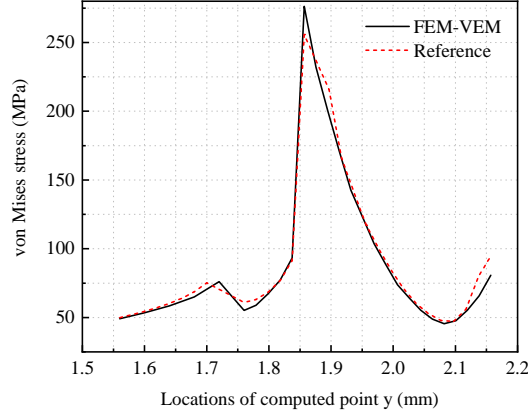


Figure 22: von Mises stress distribution along cross-material line  $L_3$ .

Fig. 22 presents the nodal stress distribution along cross-material line  $L_3$  (the blue line in Fig. 18), which traverses multiple material interfaces. The FE-VE coupling algorithm shows close agreement with the reference finite element solution across different material regions. Both methods capture the sharp stress concentration at  $y \approx 1.86$  mm, where the peak stress reaches approximately 260 MPa due to significant material property mismatches at the interface. The stress distribution ranges from approximately 50 MPa in outer regions to the 260 MPa peak, demonstrating that the coupling algorithm maintains solution continuity when transitioning between materials with different thermal and mechanical properties. These results confirm the capability of the FE-VE methodology for multi-material thermomechanical problems in electronic packaging applications.

### 5.5. IGBT Module

The final numerical example investigates the thermomechanical coupling behavior of an Insulated Gate Bipolar Transistor (IGBT) module, which represents a critical component in power electronics applications. The multi-layer IGBT structure experiences significant thermal stresses due to material

property mismatches, making thermal stress analysis essential for reliability assessment. Fig. 23 illustrates the structural configuration of the IGBT model, comprising nine distinct layers from top to bottom: Al bonding wires, Al metallized layer, IGBT chip, chip solder layer, upper Cu layers, ceramic layer, lower Cu layer, substrate solder layer, and Cu baseplate. The geometric dimensions of each component are detailed in Table 7, while the Al bonding wire geometry is shown in Fig. 24 with specific dimensions listed in Table 8. This complex multi-layer structure with curved bonding wire geometries presents an ideal test case for the FE-VE coupling methodology, where VEM's geometric flexibility effectively handles complex wire profiles while FEM efficiently manages regular substrate layers.

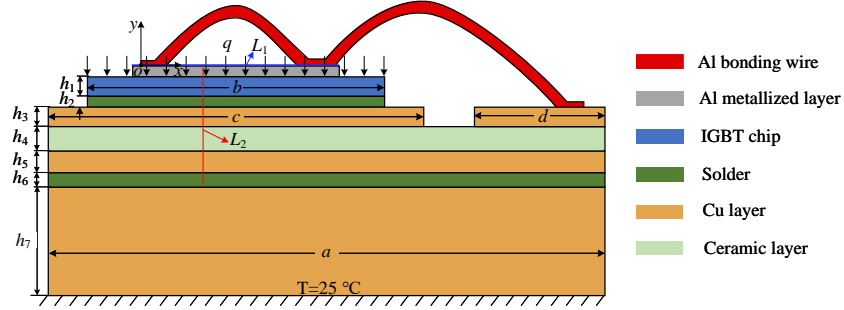


Figure 23: Geometric configuration and layer structure of IGBT module 2D model.

Table 7: Geometric dimensions of IGBT module components (mm).

Component	length	Thickness
IGBT surface Al metallized layer	11.0	0.004
IGBT chip	$b = 13.0$	$h_1 = 0.20$
IGBT chip solder layer	$b = 13.0$	$h_2 = 0.15$
Upper Cu layer 1	$c = 15.0$	$h_3 = 0.30$
Upper Cu layer 2	$d = 18.0$	$h_3 = 0.30$
Ceramic layer	$a = 18.0$	$h_4 = 0.38$
Lower Cu layer	$a = 18.0$	$h_5 = 0.30$
Substrate solder layer	$a = 18.0$	$h_6 = 0.15$
Cu baseplate	$a = 18.0$	$h_7 = 3.00$

Material parameters are assigned to each component as listed in Table 9, which reveals significant variations in thermal and mechanical characteristics that contribute to complex thermomechanical interactions. The boundary conditions simulate realistic operating conditions: a heat flux of  $q = 1000$  mW/mm<sup>2</sup> is applied to the upper surface of the IGBT chip to represent power

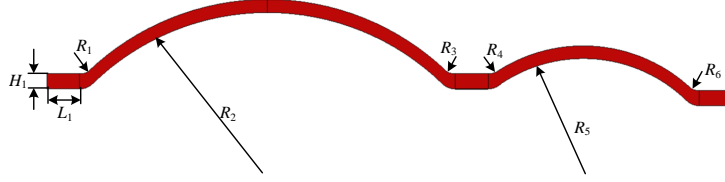


Figure 24: Geometric configuration and dimensional parameters of Al bonding wire.

Table 8: Dimensional parameters of Al bonding wire (mm).

Parameter	$H_1$	$L_1$	$R_1$	$R_2$	$R_3$	$R_4$	$R_5$	$R_6$
Dimension	0.32	0.70	0.40	5.36	0.40	0.40	3.16	0.40

dissipation during operation, the lower surface of the Cu baseplate is maintained at  $T = 25^\circ\text{C}$  representing heat sink cooling, and all remaining surfaces are treated as thermally insulated with  $\nabla T \cdot \mathbf{n} = 0$ . This configuration creates a realistic thermal gradient from the heat-generating chip through the multi-layer package structure to the cooled baseplate. The substantial differences in thermal expansion coefficients, ranging from  $2.5 \times 10^{-6} \text{ }^\circ\text{C}^{-1}$  for IGBT chip to  $22.4 \times 10^{-6} \text{ }^\circ\text{C}^{-1}$  for solder, generate significant thermal stresses that make this an excellent validation case for the FE-VE coupling methodology in handling complex multi-material electronic packaging with curved geometries and high thermal gradients.

Here, the complex Al bonding wire components are assigned to the virtual element domain, where polygonal elements facilitate mesh generation for intricate curved geometries, while the Cu baseplate is also discretized using the virtual element domain to reduce element count and computational cost. The remaining components are assigned to the finite element domain, employing four-node quadrilateral elements with careful attention to ensuring shared nodes at coupling interfaces to maintain solution continuity. Fig. 25

Table 9: Material properties of IGBT module components.

Material	Thermal conductivity (W/m·K)	Young's modulus (GPa)	Poisson's ratio	CTE $\alpha$ ( $^\circ\text{C}^{-1}$ )
Al	237	70.6	0.33	$21.0 \times 10^{-6}$
Cu	400	100	0.34	$16.4 \times 10^{-6}$
$\text{Al}_2\text{O}_3$	20	300	0.22	$6.4 \times 10^{-6}$
IGBT Chip	148	112	0.22	$2.5 \times 10^{-6}$
Solder	57	10.6	0.35	$22.4 \times 10^{-6}$

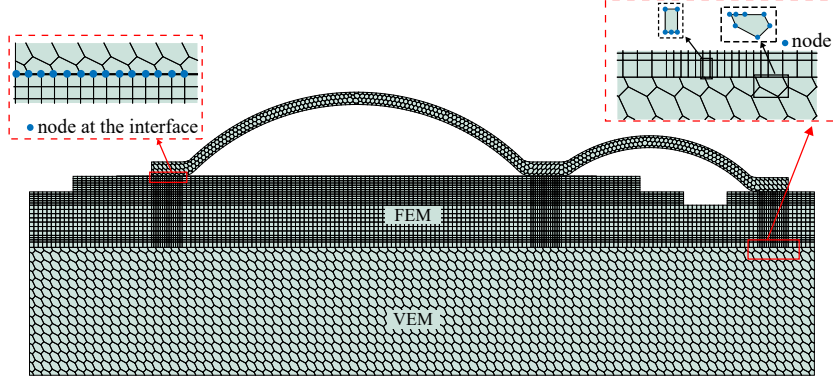


Figure 25: Hybrid mesh discretization strategy for IGBT module.

illustrates the hybrid mesh discretization strategy, demonstrating how the approach effectively combines VEM's geometric flexibility for complex wire profiles with FEM's computational efficiency for regular substrate layers. The interface regions show where nodal compatibility between VEM and FEM domains is maintained, enabling seamless integration of both numerical methods in this challenging multi-material electronic packaging configuration.

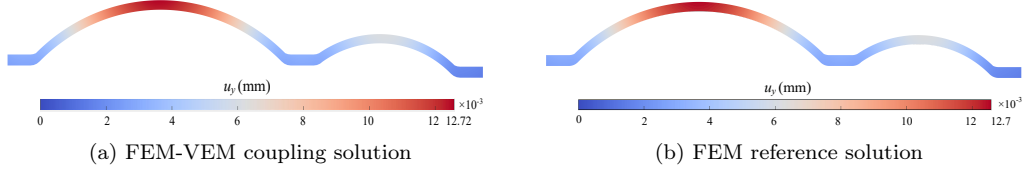


Figure 26: Vertical displacement ( $u_y$ ) distribution comparison for Al bonding wire.

Fig. 26 presents the vertical displacement distribution contours for the Al bonding wire, showing close agreement between both methods. The displacement values range from 0 to approximately 0.0126 mm for the coupling method and 0 to 0.0127 mm for the FEM method, demonstrating consistent displacement patterns throughout the complex wire geometry due to thermal expansion effects.

To provide detailed validation, nodal values were extracted along interface line  $L_1$  (the blue line in Fig. 23) using refined finite element analysis (nDof = 419,250) as the reference solution, with results presented in Fig. 27. The coupling algorithm shows good consistency across all response quantities: horizontal displacement varies linearly from  $-2.0 \times 10^{-3}$  mm to  $1.0 \times$

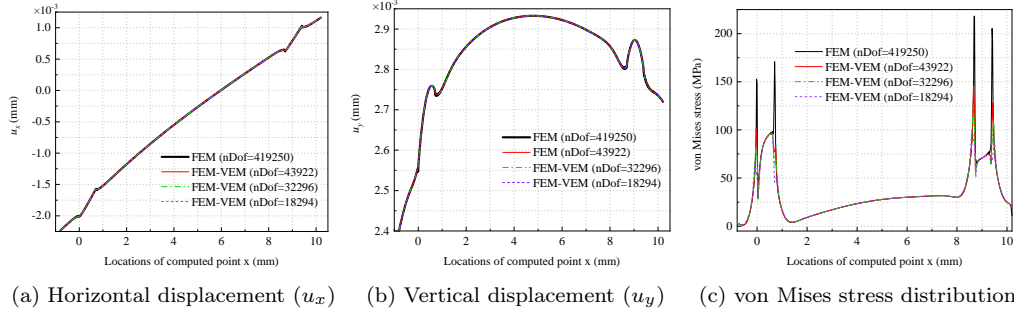


Figure 27: Displacement and stress distributions along interface line  $L_1$  (shown in Fig. 23).

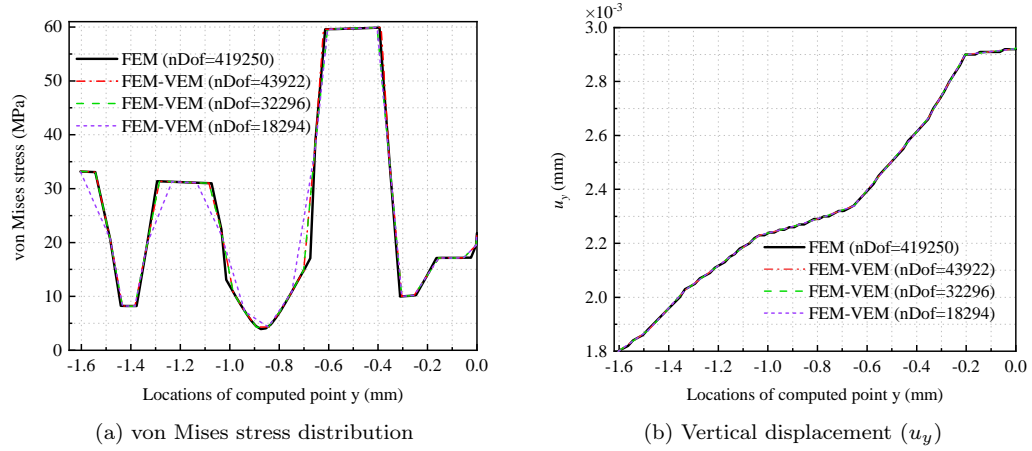


Figure 28: Stress and displacement distributions along cross-material line  $L_2$ .

$10^{-3}$  mm, vertical displacement peaks at approximately  $2.9 \times 10^{-3}$  mm, and stress distribution exhibits sharp peaks reaching 200 MPa at critical interface locations.

Fig. 28 shows results along cross-material line  $L_2$  (the red line in Fig. 23), where stress concentrations reach 60 MPa and vertical displacement varies from  $1.8 \times 10^{-4}$  mm to  $2.9 \times 10^{-4}$  mm. The coupling algorithm maintains consistency with the FEM reference solution across different mesh refinement levels, confirming the effectiveness of the proposed methodology for complex IGBT thermal stress analysis.

## 6. Conclusions

The developed FE-VE coupled method effectively captures thermal distributions and stress concentrations in multi-material systems while maintaining solution continuity across domain interfaces through strategic nodal correspondence. The approach successfully accommodates arbitrary polygonal elements in geometrically complex regions while leveraging computational efficiency in regular domains, demonstrating consistent performance across different mesh refinement levels. Validation through comprehensive numerical examples spanning sintered silver interconnects, FC-BGA packages, and IGBT modules demonstrates reasonable agreement with reference solutions and acceptable convergence characteristics. The coupled method maintains adequate computational precision while providing practical advantages through strategic domain partitioning, establishing a viable computational framework for thermomechanical analysis of electronic packaging structures with complex multi-scale geometries.

This FE-VE coupled framework advances computational mechanics by providing enhanced flexibility for analyzing electronic packaging technologies with complex geometric features. Future research directions include: (i) extending the approach to 3D thermomechanical problems, (ii) incorporating more sophisticated material models including plasticity and damage mechanics, (iii) investigating adaptive mesh refinement strategies for optimal domain partitioning, and (iv) developing fully coupled solutions for strongly bidirectional thermomechanical interactions. To facilitate reproducibility and further development, source codes and implementation examples are publicly available at <https://github.com/yanpeng-gong/FeVeCoupled-ElectronicPackaging>.

## Acknowledgments

This research was supported by the National Natural Science Foundation of China (No. 12002009).

## References

- [1] C. Xiao, H. He, J. Li, S. Cao, W. Zhu, An effective and efficient numerical method for thermal management in 3D stacked integrated circuits, *Applied Thermal Engineering* 121 (2017) 200–209. doi:<https://doi.org/10.1016/j.applthermaleng.2017.04.080>.
- [2] B. Li, M. Tang, J. Mao, An efficient LBFEM-POD scheme for transient thermomechanical simulation of electronic packages, *IEEE Transactions on Components, Packaging and Manufacturing Technology* (2024). doi:[10.1109/TCPMT.2024.3435867](https://doi.org/10.1109/TCPMT.2024.3435867).
- [3] Y. Gong, Y. Kou, Q. Yue, X. Zhuang, F. Qin, Q. Wang, T. Rabczuk, The application of thermomechanically coupled phase-field models in electronic packaging interconnect structures, *International Communications in Heat and Mass Transfer* 159 (2024) 108033. doi:<https://doi.org/10.1016/j.icheatmasstransfer.2024.108033>.
- [4] F. Su, W.-J. Li, T.-B. Lan, W. Shang, Investigation on hygro-thermo-mechanical stress of a plastic electronic package, *Journal of Mechanics* 30 (6) (2014) 625–630. doi:<https://doi.org/10.1017/jmech.2014.52>.
- [5] Z. He, Y. Yan, Z. Zhang, Thermal management and temperature uniformity enhancement of electronic devices by micro heat sinks: A review, *Energy* 216 (2021) 119223. doi:<https://doi.org/10.1016/j.energy.2020.119223>.
- [6] G. Ye, X. Fan, G. Zhang, Practical aspects of thermomechanical modeling in electronics packaging: A case study with a SiC power package, *Microelectronics Reliability* 132 (2022) 114514. doi:<https://doi.org/10.1016/j.microrel.2022.114514>.
- [7] J. Vallepuga-Espinosa, I. Ubero-Martínez, L. Rodríguez-Tembleque, J. Cifuentes-Rodríguez, A boundary element procedure to analyze

- the thermomechanical contact problem in 3d microelectronic packaging, *Engineering Analysis with Boundary Elements* 115 (2020) 28–39. doi:<https://doi.org/10.1016/j.enganabound.2020.02.011>.
- [8] H. Yu, Y. Guo, Y. Gong, F. Qin, Thermal analysis of electronic packaging structure using isogeometric boundary element method, *Engineering Analysis with Boundary Elements* 128 (2021) 195–202. doi:<https://doi.org/10.1016/j.enganabound.2021.04.008>.
- [9] Y. Gong, F. Qin, C. Dong, J. Trevelyan, An isogeometric boundary element method for heat transfer problems of multiscale structures in electronic packaging with arbitrary heat sources, *Applied Mathematical Modelling* 109 (2022) 161–185. doi:<https://doi.org/10.1016/j.apm.2022.03.047>.
- [10] Y. Gong, Y. He, H. Hu, X. Zhuang, F. Qin, H. Xu, T. Rabczuk, A coupled finite element-boundary element method for transient elastic dynamic analysis of electronic packaging structures, *Engineering Structures* 326 (2025) 119500. doi:<https://doi.org/10.1016/j.engstruct.2024.119500>.
- [11] F. Qin, Q. He, Y. Gong, T. An, P. Chen, Y. Dai, The application of FEM-BEM coupling method for steady 2D heat transfer problems with multi-scale structure, *Engineering Analysis with Boundary Elements* 137 (2022) 78–90. doi:<https://doi.org/10.1016/j.enganabound.2022.01.009>.
- [12] Y. Gong, Y. Kou, Q. Yue, X. Zhuang, N. Valizadeh, F. Qin, Q. Wang, T. Rabczuk, A phase-field study on thermo-mechanical coupled damage evolution and failure mechanisms of sintered silver interconnections, *Engineering Fracture Mechanics* 320 (2025) 111039. doi:<https://doi.org/10.1016/j.engfracmech.2025.111039>.
- [13] X. Long, J. Zhu, Y. Su, Y. Yan, C. Chang, H. Zhang, V. Salomoni, Phase field fracture modeling of mechanical degradation and crack propagation in random porous sintered nano-silver with thermal and strain-rate effects, *Engineering Fracture Mechanics* 314 (2025) 110753. doi:<https://doi.org/10.1016/j.engfracmech.2024.110753>.  
URL <https://www.sciencedirect.com/science/article/pii/S0013794424009160>



- [14] Y. Gong, Y. He, Y. Mei, X. Zhuang, F. Qin, T. Rabczuk, Physics-informed kolmogorov-arnold networks for multi-material elasticity problems in electronic packaging (2025). arXiv:2508.16999.  
URL <https://arxiv.org/abs/2508.16999>
- [15] T. Raszkowski, M. Zubert, Analysis of algorithm efficiency for heat diffusion at nanoscale based on a MEMS structure investigation, *Energies* 13 (10) (2020) 2520. doi:<https://doi.org/10.3390/en13102520>.
- [16] C. Khor, M. Abdullah, M. A. Mujeebu, F. C. Ani, FVM based numerical study on the effect of solder bump arrangement on capillary driven flip chip underfill process, *International Communications in Heat and Mass Transfer* 37 (3) (2010) 281–286. doi:<https://doi.org/10.1016/j.icheatmasstransfer.2009.11.012>.
- [17] A. Inamdar, M. van Soestbergen, A. Mavinkurve, W. van Driel, G. Zhang, Modelling thermomechanical degradation of moulded electronic packages using physics-based digital twin, *Microelectronics Reliability* 157 (2024) 115416. doi:<https://doi.org/10.1016/j.microrel.2024.115416>.
- [18] S. Feng, Y. Guo, G. Królczyk, X. Han, A. Incecik, Z. Li, An engineered solution to multi-physics of insulated gate bipolar transistor module considering electrical-thermal-mechanical coupling effect, *Advances in Engineering Software* 175 (2023) 103365. doi:<https://doi.org/10.1016/j.advengsoft.2022.103365>.
- [19] H. Wang, J. Ma, M. Gong, P. Su, Structural optimization of thermal stresses in BGA solder joints based on improved BP neural network-genetic algorithm, *The European Physical Journal Plus* 138 (8) (2023) 712. doi:<https://doi.org/10.1140/epjp/s13360-023-04355-w>.
- [20] J. Wang, Y. Deng, Z. Zhang, J. Jin, P. Liu, Thermal stress behavior and optimization of solder joints in CSP-LED packages, *Results in Engineering* 26 (2025) 104712. doi:<https://doi.org/10.1016/j.rineng.2025.104712>.
- [21] Q. Q. Liu, M. Zhuang, W. Zhan, N. Liu, Q. H. Liu, An efficient thin layer equivalent technique of SETD method for thermo-mechanical multi-physics analysis of electronic devices, *International Journal of Heat and Mass Transfer* 192 (2022) 122816. doi:<https://doi.org/10.1016/j.ijheatmasstransfer.2022.122816>.

- [22] L. Gong, Y.-P. Xu, B. Ding, Z.-H. Zhang, Z.-Q. Huang, Thermal management and structural parameters optimization of MCM-BGA 3D package model, *International Journal of Thermal Sciences* 147 (2020) 106120. doi:<https://doi.org/10.1016/j.ijthermalsci.2019.106120>.
- [23] Y. Xia, Y. Su, X. Xu, L. Ju, R. Zhang, Y. Xue, Y. Liu, S. Zhang, Effect of thermal cycling on the strain and stress distribution of TSVs and solder bumps in stacked package structure, *e-Prime-Advances in Electrical Engineering, Electronics and Energy* 5 (2023) 100274. doi:<https://doi.org/10.1016/j.prime.2023.100274>.
- [24] Y. Gong, S. Li, F. Qin, B. Xu, Virtual element method for thermo-mechanical analysis of electronic packaging structures with multi-scale features (2025). arXiv:2508.11410. URL <https://arxiv.org/abs/2508.11410>
- [25] L. Beirão da Veiga, F. Brezzi, A. Cangiani, G. Manzini, L. D. Marini, A. Russo, Basic principles of virtual element methods, *Mathematical Models and Methods in Applied Sciences* 23 (01) (2013) 199–214. doi:<https://doi.org/10.1142/S0218202512500492>.
- [26] E. Artioli, L. Beirão da Veiga, C. Lovadina, E. Sacco, Arbitrary order 2D virtual elements for polygonal meshes: part I, elastic problem, *Computational Mechanics* 60 (2017) 355–377. doi:<https://doi.org/10.1007/s00466-017-1404-5>.
- [27] T. Sorgente, S. Biasotti, G. Manzini, M. Spagnuolo, The role of mesh quality and mesh quality indicators in the virtual element method, *Advances in Computational Mathematics* 48 (1) (2022) 3. doi:<https://doi.org/10.1007/s10444-021-09913-3>.
- [28] T. Sorgente, S. Biasotti, G. Manzini, M. Spagnuolo, Polyhedral mesh quality indicator for the virtual element method, *Computers & Mathematics with Applications* 114 (2022) 151–160. doi:<https://doi.org/10.1016/j.camwa.2022.03.042>.
- [29] D. van Huyssteen, B. Reddy, A virtual element method for isotropic hyperelasticity, *Computer Methods in Applied Mechanics and Engineering* 367 (2020) 113134. doi:<https://doi.org/10.1016/j.cma.2020.113134>.

- [30] D. van Huyssteen, B. Reddy, A virtual element method for transversely isotropic hyperelasticity, *Computer Methods in Applied Mechanics and Engineering* 386 (2021) 114108. doi:<https://doi.org/10.1016/j.cma.2021.114108>.
- [31] B.-B. Xu, W.-L. Fan, P. Wriggers, High-order 3D virtual element method for linear and nonlinear elasticity, *Computer Methods in Applied Mechanics and Engineering* 431 (2024) 117258. doi:<https://doi.org/10.1016/j.cma.2024.117258>.
- [32] H. Chi, L. Beirão Da Veiga, G. H. Paulino, Some basic formulations of the virtual element method (VEM) for finite deformations, *Computer Methods in Applied Mechanics and Engineering* 318 (2017) 148–192. doi:<https://doi.org/10.1016/j.cma.2016.12.020>.
- [33] W. Shen, M. Ohsaki, J. Zhang, A 2-dimentional contact analysis using second-order virtual element method, *Computational Mechanics* 70 (2) (2022) 225–245. doi:<https://doi.org/10.1007/s00466-022-02165-y>.
- [34] M. Cihan, B. Hudobivnik, J. Korelc, P. Wriggers, A virtual element method for 3D contact problems with non-conforming meshes, *Computer Methods in Applied Mechanics and Engineering* 402 (2022) 115385. doi:<https://doi.org/10.1016/j.cma.2022.115385>.
- [35] B. Hudobivnik, F. Aldakheel, P. Wriggers, A low order 3D virtual element formulation for finite elasto-plastic deformations, *Computational Mechanics* 63 (2019) 253–269. doi:<https://doi.org/10.1007/s00466-018-1593-6>.
- [36] P. Wriggers, B. Hudobivnik, A low order virtual element formulation for finite elasto-plastic deformations, *Computer Methods in Applied Mechanics and Engineering* 327 (2017) 459–477. doi:<https://doi.org/10.1016/j.cma.2017.08.053>.
- [37] T.-R. Liu, F. Aldakheel, M. Aliabadi, Virtual element method for phase field modeling of dynamic fracture, *Computer Methods in Applied Mechanics and Engineering* 411 (2023) 116050. doi:<https://doi.org/10.1016/j.cma.2023.116050>.
- [38] V. Dhanush, S. Natarajan, Implementation of the virtual element method for coupled thermo-elasticity in Abaqus, *Numerical Algorithms*

- 80 (3) (2019) 1037–1058. doi:<https://doi.org/10.1007/s11075-018-0516-0>.
- [39] P. W. Bing-Bing Xu, 3d stabilization-free virtual element method for linear elastic analysis, *Computer Methods in Applied Mechanics and Engineering* 421 (2024) 116826. doi:<https://doi.org/10.1016/j.cma.2024.116826>.
  - [40] H. B. Wriggers P, Aldakheel F, *Virtual element methods in engineering sciences*, Berlin/Heidelberg, Germany: Springer, 2024.
  - [41] M. Mengolini, M. F. Benedetto, A. M. Aragón, An engineering perspective to the virtual element method and its interplay with the standard finite element method, *Computer Methods in Applied Mechanics and Engineering* 350 (2019) 995–1023. doi:<https://doi.org/10.1016/j.cma.2019.02.043>.
  - [42] C. Herrera, R. Corrales-Barquero, J. Arroyo-Esquivel, J. G. Calvo, A numerical implementation for the high-order 2D virtual element method in MATLAB, *Numerical Algorithms* 92 (3) (2023) 1707–1721. doi:[10.1007/s11075-022-01361-4](https://doi.org/10.1007/s11075-022-01361-4).
  - [43] A. Chen, N. Sukumar, Stabilization-free virtual element method for plane elasticity, *Computers & Mathematics with Applications* 138 (2023) 88–105. doi:<https://doi.org/10.1016/j.camwa.2023.03.002>.
  - [44] K. Berbatov, B. Lazarov, A. Jivkov, A guide to the finite and virtual element methods for elasticity, *Applied Numerical Mathematics* 169 (2021) 351–395. doi:<https://doi.org/10.1016/j.apnum.2021.07.010>.
  - [45] B.-B. Xu, F. Peng, P. Wriggers, Stabilization-free virtual element method for finite strain applications, *Computer Methods in Applied Mechanics and Engineering* 417 (2023) 116555. doi:<https://doi.org/10.1016/j.cma.2023.116555>.